Effect of pressure on the deformation of quartz aggregates in the presence of H_2O

L. Nègre, H. Stünitz, H. Raimbourg, A. Lee, J. Précigout, P. Pongrac, P. Jeřábek

PII: S0191-8141(21)00075-4

DOI: https://doi.org/10.1016/j.jsg.2021.104351

Reference: SG 104351

To appear in: *Journal of Structural Geology*

Received Date: 8 December 2020

Revised Date: 9 April 2021

Accepted Date: 13 April 2021

Please cite this article as: Nègre, L., Stünitz, H., Raimbourg, H., Lee, A., Précigout, J., Pongrac, P., Jeřábek, P., Effect of pressure on the deformation of quartz aggregates in the presence of H_2O, *Journal of Structural Geology*, https://doi.org/10.1016/j.jsg.2021.104351.

Author statement

All authors have read the manuscript and agree with its content.

Effect of pressure on the deformation of quartz aggregates in the presence of H_2O

Authors: L. Nègre [a,*], H. Stünitz [a,b], H. Raimbourg [a], A. Lee [b], J. Précigout [a], P. Pongrac [c], P. Jeřábek [c]

[a] Institut des Sciences de la Terre d'Orléans (ISTO), UMR 7327, CNRS/BRGM, Université d'Orléans, 45071 Orléans, France

[b] Department of Geology, University of Tromsø, Dramsveien 201, 9037 Tromsø, Norway

[c] Institute of Petrology and Structural Geology, Faculty of Science, Charles University in Prague, Albertov 6, 128 43 Prague, Czech Republic

Email adresses: lucille.negre@univ-orleans.fr (L. Nègre), holger.stunitz@uit.no (H. Stünitz), hugues.raimbourg@univ-orleans.fr (H. Raimbourg), amicia.lee@uit.no (A. Lee), jacques.precigout@univ-orleans.fr (J. Précigout), petar.pongrac@natur.cuni.cz (P. Pongrac), jerabek.petr@natur.cuni.cz (P. Jeřábek)

Corresponding author: Institut des Sciences de la Terre d'Orléans (ISTO), 1a rue de la Férollerie, 45100 Orléans, France, +332 38 25 50 27

Keywords: quartz deformation, quartz rheology, H_2O weakening, dynamic recrystallization

Abstract

Quartzite samples of high purity with a grain size of ~200 μm have been experimentally deformed by coaxial shortening in a solid medium apparatus at 900°C and at confining pressures ranging from 0.6 to 2 GPa. Most samples have been shortened by ~30% with 0.1 wt.% added H_2O. The samples deformed dominantly by crystal plasticity (dislocation creep), and there is a systematic decrease of flow stress with increasing confining pressure. Strain rate stepping tests yield stress exponents of n~1.4. The strain determined from individual grain shapes matches that determined from bulk shortening. In addition to plastic strain, mode I cracks developed in all samples, principally in the grain boundary regions. Recrystallized material, visible through cathodoluminescence colours, forms by two mechanisms: (1) progressive subgrain rotation and (2) cracking, nucleating small new grains. After high-angle boundaries have been established, grain boundary migration takes place, and a distinction of new grains nucleation origin (subgrain rotation or cracking) is impossible. At higher pressure, there is more recrystallized material forming in the deformed samples, and it is inferred that the inverse pressure dependence of flow stress is caused by enhanced grain boundary migration at higher pressure, consistent with previous studies.

1. Introduction

Despite a long history of research since the early discovery of the effect of H_2O on quartz rheology by Griggs and Blacic (1965), many aspects of H_2O weakening in quartz are yet unresolved. One of these aspects is the clearly observed dependence of the H_2O weakening on pressure: it had been suggested by Paterson and Kekulawala, (1979), Tullis et al. (1979), Blacic (1981) and Mainprice and Paterson (1984) that the confining pressure has an enhancing effect on the H_2O weakening effect in quartz, speculating that pressure may positively affect the diffusive uptake of H_2O. The seminal work by Kronenberg and Tullis (1984) clearly demonstrated and quantified the increasing weakening of quartzite with increasing confining pressure in the presence of H_2O. However, not much later it has been shown by Kronenberg et al. (1986) and Gerretsen et al. (1989) that the diffusion of H_2O into quartz occurs at rates far too slow (or not at all) to play a role in deformation experiments, and that the infiltration of H_2O into quartz is achieved by microcracking in experiments. Thus, the effect of pressure on deformation of quartz in the presence of H_2O had been demonstrated but its cause was not very clear. Tullis and Yund (1989) have presented a study of annealing deformed quartz crystals at different pressures in the presence of H_2O and have shown that recovery and recrystallization are enhanced by higher pressures.

In more recent studies of fine grained quartz material Rutter and Brodie (2004a,b) have determined stress exponents of $n \approx 3$ and $n = 1$ and have demonstrated grain size sensitive flow in quartz. These n-values are lower than previous n-values of $n = 4$ determined by Paterson and Luan (1990) and Luan and Paterson (1992) for dislocation creep. Fukuda et al. (2018) and Richter et al. (2018) have determined n-values of 1.7 to 1.9, respectively. These values were partly interpreted as a combination of dislocation and diffusion creep mechanisms. As the experiments of

Kronenberg and Tullis (1984) have been carried out using fine grained novaculite, and as this material has also been used in the experiments by Fukuda et al. (2018), it appears likely that the pressure dependence of deformation has been determined in material partially deformed by diffusion creep processes in the presence of H_2O. The solubility of quartz in supercritical H_2O increases non-linearly with increasing pressure (Manning, 1994, 2018), so that solution-precipitation processes may be expected to be enhanced at high pressures. Diffusion creep in the presence of H_2O will involve dissolution and precipitation and therefore is expected to be pressure dependent. The pressure dependence of quartz rheology could therefore arise from enhanced dissolution at higher pressures. For this reason, we have revisited the pressure dependence of quartz deformation using a coarser grained quartzite (~200 µm grain size) as starting material in order to diminish the role of diffusion creep processes and to test whether the dependence of quartz strength on pressure is the same as in fine grained material and to study the processes of weakening in more detail.

2. Methods

2.1 Deformation experiments

Coaxial shortening deformation experiments of natural quartzite (for the characterization of the starting material see the results-section) have been performed in two types of solid medium apparatus (a modified Griggs apparatus at University of Tromsø, Norway and a new generation solid medium apparatus at ISTO, Orléans, France). NaCl was used as the confining medium in both sets of experiments. The preparation procedure followed for samples deformed in Orléans corresponds to the one described by Précigout et al. (2018). For samples deformed in Tromsø, assemblies differ in size (smaller diameter and length) and use a single thermocouple instead of two.

Cylindrical samples (diameter 6.35 mm for samples in the conventional Griggs apparatus in Tromsø and 8 mm for the new rig in Orléans) were cored from the starting material (without any preferential orientation), with ends ground flat and plane-parallel to ~0.001 mm tolerance. They were dried at 110°C for one day (minimum), then weighed, wrapped with two layers of nickel foil (0.025 mm thickness), inserted into platinum jacket (0.15 mm thickness) and weld-sealed after addition of 0.1 wt.% of distilled water.

For deformation experiments at 2 GPa confining pressure, the sample assembly was slightly modified. The top piston and top inner salt piece were separated into two parts and a disc of compressed salt (of approximately 2.6 mm thickness and 13 mm diameter) was inserted in between. In this way, the deformation column was able to compact as P and T were increased to the final P-T conditions of the experiment without applying much deviatoric stress on the sample when advancing the pistons. Before this modification of the sample assembly, several experiments failed as the hit-point was reached during the pumping stage and the sample started to deform earlier than expected.

All deformation experiments have been performed to approximately 30% coaxial shortening (total strain of samples is between ~26 and 33%, except for the high-strain OR56 sample of ~74%) at a temperature of 900°C and constant strain rate of approximatively 10^{-6} s^{-1} – corresponding to a constant displacement rate of 1.5 x 10^{-5} $mm.s^{-1}$ (Table 2). The strain rate of experiments in the rig at Orléans was slightly lower (by ~30%) than in the Tromsø rig. However, for a power law solid, this difference in strain rate should lead to only a subtle difference in flow stress. Confining pressures were 600, 700, 800, 1000, 1250, 1500 and 2000 MPa (Table 2). In the new type of solid medium apparatus, the pressure is regulated by a hydraulic pump and remains constant throughout the experiment, whereas in the conventional

Griggs apparatus, it is not regulated and typically increases towards the end of the experiment (the increase is corrected in the mechanical record).

One sample (OR56) was deformed at 2000 MPa at a faster strain rate of $\sim 10^{-5}$ s^{-1} (1.5 x 10^{-4} $mm.s^{-1}$) and shortened by 70%. As the hit point was reached during the pumping phase, the strength of this sample could not be determined.

Two strain rate stepping experiments have been performed in order to determine the n-exponent of the flow law. During these experiments, the pressure (2000 MPa for OR68 and 800 MPa for OR79) and temperature (900°C) conditions were kept constant but the strain rate was changed. For both experiments, the strain rate sequence was $\sim$1 x 10^{-5}, 10^{-7}, 10^{-6} and 10^{-5} s^{-1}. The n-exponent was then defined for each experiment as the slope between the log of the strain rates at the end of each strain rate step and the log of the differential stresses calculated by linear regression.

Processing of the mechanical data was carried out with a MATLAB program (Pec et al., 2016) adapted by J. Précigout following the routines of Heilbronner (https://micro.earth.unibas.ch). Finite strain of the deformed samples was calculated from mechanical record and from direct measurements of samples lengths before and after the experiments.

After the experiments, all samples were cut through the centre with a diamond saw (passing through the thermocouple positions) to obtain a longitudinal section parallel to the sigma 1 direction. Thin (30 µm) and thick (90 and 150 µm) sections have been prepared from the two parts.

2.2 Cathodoluminescence

Cathodoluminescence (CL) imaging has been carried out on samples using the light microscope (LM) and the scanning electron microscope (SEM). LM-CL-images

of thin sections have been recorded at ISTO (Orléans) with an OPEA cold cathode stage at approximately 10-12 kV and 120-150 µA under low-pressure Argon gas at 6.7 to 7.3 Pa. The image acquisition time was 3 to 4 s. SEM-CL-images have been recorded at BRGM (Orléans) with EDAX-Pegasus system equipped with a TESCAN CL-detector. Conditions of imaging were 5 to 15 kV and 17 to 20 mm working distance. Prior to analysis, samples were coated with 20 nm of carbon. Additional mosaic CL-images have been recorded at the University of Tromsø using a Gatan Mono-CL-system on a Zeiss Merlin Compact SEM at 15 kV and 12.5 to 13.7 mm working distance using a blue filter (380-515 nm). These images have been manually segmented and processed using ImageJ software.

2.3 Bulk sample strain analysis from sand grain shapes

Cathodoluminescence and plane polarized light microscopy allow to identify the original sand grains of the Tana quartzite and to distinguish them from the cement. Light microscope (cross-polarized and cathodoluminescence) mosaic images of the starting material and of samples deformed at different pressures have been manually segmented to isolate original sand grains. These sand grains have been analysed using the open-source *ImageJ* program to obtain statistics on grain parameters (cross section area, shape, orientation) as described by Heilbronner and Barrett (2013).

The sand grain size is expressed as the equivalent diameter (d_{eq}) calculated from the area of grains (A) as $d_{eq} = 2 \times \sqrt{\frac{A}{\pi}}$. The fabric is expressed as the aspect ratio (AR), the mean ratio between the long (a) and short (b) axes of the particles ($AR = \frac{a}{b}$) and their orientation. The dataset has been analysed by the SURFOR method described by Panozzo (1984) in *ImageJ* for a fabric and strain analysis.

2.4 Electron Backscatter Diffraction (EBSD) analysis

Crystal orientations have been determined by electron backscatter diffraction (EBSD) using a Nordlys detector and an Oxford Aztec system on a Zeiss Merlin Compact FE-SEM at the University of Tromsø using a 70° tilt angle, 20 kV acceleration voltage, and 9 nA probe current. An indexing quote of 75-85% has been achieved on 4 nm carbon coated thin sections. Post-processing was performed using the MTEX v.5.2.8 program package by Bachmann et al. (2010). Orientation maps were recalculated using the 6/mmm system (hexagonal) in order to avoid displaying Dauphiné twin boundaries.

2.5 Fourier Transform Infrared (FTIR) Spectroscopy

Double-polished thick sections of 150 and 90 µm have been prepared from the starting material and Fourier transform infrared spectroscopy (FTIR) analysis has been performed at ISTO (Orléans) with Nicolet 6700 (Continµum, Thermoscientific) spectrometer and OMNIC (version 8) acquisition software.

The spectra were acquired on grain interiors, grain boundaries, and cement with 64 and 128 scans and a resolution of 4 cm^{-1} for a range of wave numbers from 5500 to 1500 cm^{-1}. A window with 40x40 µm for interior of grains and with 20x50 µm was used for grain boundary measurements (window shape and orientation was adapted to the boundaries). The background was recorded for the CaF_2 window carrying the sample and subtracted from the measured spectra. Water contents were calculated using the Beer-Lambert law and the Paterson (1982) calibration.

2.6 Water fugacity calculations

Assuming that during the experiments the H_2O pressure approximatively equals the confining pressure, the water fugacity (f_{H2O}) can be calculated using only two parameters: the temperature and the pressure. The water fugacity has been computed

for all experimental conditions from Tony Withers' fugacity calculator (available at: https://www.esci.umn.edu/people/researchers/withe012/fugacity.htm) based on the Pitzer and Sterner (1994) equation of state for water.

3. Results

3.1 Starting material

For the starting material, a very pure natural quartzite from the ELKEM quarry in Austertana, Northern Norway (N70°28´39.6´´, E28°32´30.1´´) has been used. The rock samples come from the top part (~40 m) of the Gamasfjell formation. This sequence of late Precambrian age is approximatively 300 m thick and its top part is composed of grey to white quartzite (Pevik, 2015). The uppermost part of the formation is described as very pure (> 99% of silica), and used by the aluminium, silicon, and ferrosilicon industry (Aasly et al., 2007). Chemical analysis (from ICP-EOS) published in Pevik (2015) indicate major oxide values (apart from SiO_2) of 3547 ± 1083 ppm Al_2O_3, 441 ± 365 ppm Fe_2O_3, and 207 ± 37 ppm TiO_2.

The Tana quartzite underwent high grade diagenesis to very low grade metamorphic conditions and is weakly deformed in a large open antiform (Pevik, 2015). However, no internal deformation on the micro-scale, no schistosity, and no lineation have been identified in the sampled rock. The blocks of the starting material collected were not oriented. The quartzite is composed of quartz grains and crystalline authigenic SiO_2 cement (99%, Fig. 1a) and very few accessory minerals (< 1%) such as sheet silicates (sericite, pyrophyllite, kaolinite), iron oxides (hematite), zircons, apatite, xenotime, monazite, rutile, and very rare feldspars. Due to filling of the pore space by authigenic SiO_2 cement, no visible porosity was detected in the light microscope or SEM.

Microstructural analysis and CL-imaging show that the quartz grains forming the

Tana quartzite are composed of (1) cores of equant and rounded detrital quartz sand grains, with various CL-colours and -intensity, and (2) a non- or dark-luminescent cement between the grains (Fig. 1c,d). The cement is in crystallographic continuity with the sand grains on which it grows epitaxially (Fig. 1a). Grains appear undeformed as they do not show any undulatory extinction, except for rare sand grains showing inherited recrystallized microstructures. A few pressure-solution contacts due to burial of the sediment are sometimes observed.

The size distribution of quartz grains composing the quartzite was obtained by image analysis using both polarized light and light microscopy (LM)-CL-images. The mean grain size is 204 µm for quartz grains and 186 µm for original sand grains (Table 1). The quartz grain sizes are larger than those of sand grains because they include the surrounding cement. The calculated mean aspect ratio (AR) is 1.56 for quartz grains and 1.55 for sand grains, indicating that grains are somewhat elongated. However, no preferred orientation of the long axes of the grains can be detected. For this reason, samples have been cored without reference to any specific orientation.

Electron Backscatter Diffraction (EBSD) measurements of grains from starting material Tana quartzite (one point per grain, n=500) confirm a random fabric (Fig. 1b, with J=1.33 and M=0.027), close to a random distribution (Bunge, 1982; Skemer et al., 2005). The dislocation density of the material was characterized by transmission electron microscopy (TEM) as 6 $x10^{12}$ m^{-2}, which is a typical, low dislocation density of relatively undeformed natural silicates (McLaren, 2005).

The mean water content calculated is 1659 H/10^6 Si for grain interiors and 2120 H/10^6 Si for grain boundaries.

3.2 Mechanical data

3.2.1 Stress strain curves

The samples show a systematic decrease in strength with increasing confining pressure (Fig. 2): the maximum final differential stress is nearly 600 MPa for a sample deformed at 600 MPa confining pressure, whereas for the sample deformed at 2000 MPa it is ~100 MPa. This behaviour is reproducible for the two different apparatus (considering a ± 30 MPa accuracy of the solid medium apparatus; Holyoke and Kronenberg, 2010) used for a confining pressure of 1000 MPa (samples 546LN and OR32; the strain rate is slightly lower in OR32) whereas for lower pressure at 600 MPa, the sample deformed in Orléans (OR60) is slightly stronger than the one in Tromsø (542LN), despite the slightly slower strain rate.

3.2.2 Strain rate stepping experiments

Two strain rate stepping experiments were performed at high (OR68, 2000 MPa) and low (OR79, 800 MPa) pressures to determine the n-value, or the stress exponent, of the flow law. Both experiments were conducted at 900°C with 0.1 wt.% water added and with a strain rate sequence of $\sim 10^{-5}$, $\sim 10^{-6}$, $\sim 10^{-7}$ then again $\sim 10^{-5}$ s^{-1}. The stress-strain-curves are presented in Fig. 3a and flow stresses for each step are reported in Table 3.

The initial step at $\sim 10^{-5}$ s^{-1} has been repeated at the end of the experiments for a test of reproducibility. The flow stresses associated to that rate are systematically higher during the final step and steady state has not really been reached for the lower confining pressure experiment. For the steps at $\sim 10^{-7}$ s^{-1}, both samples show an unstable and variable behaviour, probably due to the low sample strength, so that possibly some friction effects at the pistons start to play a role. In addition, at such low strain rates the initial “friction” of the run-in curve is partially recovered, so that the recorded stresses may be too low (see explanation of this effect in Tarantola et

al., 2012, appendix). In the next generation Sanchez apparatus, very low oil flow is injected by the hydraulic pump (0.0007 mL/min) in order to obtain this strain rate, this variation may partially reflect changes in the ambient conditions (daily variations recorded for the force, influenced by room temperature or cooling temperature variations).

The n-exponent is defined as the slope of the linear regression in the log-log plot of the flow stresses vs. strain rate (Fig. 3b). For the low pressure experiment (OR79, 800 MPa), n∼1.42 is obtained, and for the high pressure one (OR68, 2000 MPa), n∼1.40. Given the uncertainties of the stress determination in the solid medium apparatus, these n-values are identical. If the slowest strain rate steps are omitted as somewhat less reliable (see above), the resulting n-values are 2.33 for 2000 MPa and 1.96 for 800 MPa confining pressure.

3.3 Microstructures

3.3.1 Light microscopy

The local strain distribution in all samples is inhomogeneous. Typically, the centre and/or bottom parts of the samples are more strongly deformed (Fig. 4). The partitioning of deformation typically is detected by more elongated grain shapes in the higher strained regions (Fig. 4b). The greater elongation of individual quartz grains usually is accompanied by an increase in the amount of recrystallized material. Original quartz grains in deformed samples show evidence for plastic deformation, such as undulatory extinction, deformation lamellae and, in some places, development of subgrains (observed in the LM; Fig. 4c). Some of the progressive subgrain rotation leads to the formation of core-mantle structures (Fig. 4b,c).

This strain gradient is slightly more pronounced for samples deformed in the

290 conventional Griggs apparatus at Tromsø (where more of the deformation is
291 localized at the lower part of the samples) than for those deformed in the new
292 apparatus in Orléans (where more of the deformation is located in the central part of
293 the sample). This type of strain localisation is common in samples deformed in the
294 solid medium apparatus (e.g., Heilbronner, 2002; Heilbronner and Tullis, 2002;
295 Stünitz et al., 2017) and is related to the temperature gradient in the sample. The
296 thermocouple position indicates the highest temperature of the sample (< 90°C
297 temperature difference between sample ends and the hot zone = thermocouple
298 position) and this region typically corresponds to the higher strain regions.

299 *3.3.2 Cathodoluminescence*

300 SEM-CL and LM-CL images show that in all deformed samples the original sand
301 grains can still be identified by the same variation of luminescence and tints as in the
302 starting material (Figs. 1 & 5). The sand grains in the more highly deformed parts of
303 the sample show a more elongated shape with the long axis at a large angle or
304 normal to the shortening direction. In the cemented area between the original sand
305 grains, the darker luminescent cement is clearly observable. However, in the
306 deformed samples, a new material with a bright luminescence appears in CL-images
307 (Figs. 5 & 6). This bright luminescence material invariably has a blue colour, so that
308 a blue filter was used in SEM-CL images to enhance its presence. The blue
309 luminescence is not short-lived but permanent.

310 *3.3.2.1 Morphology of the bright luminescent material*

311 The bright luminescence material in deformed samples is often concentrated in
312 the boundary regions of grains, so that these bright regions appear predominantly in
313 the cement at the grain boundaries of quartz grains. In some cases the bright
314 luminescing material cuts across original sand grains (Fig. 6a,b). In the low strain
315 parts of the samples, the brightly luminescing zones follow a clear crack morphology

316 (Figs. 5 & 6). The bright luminescent material occurs in the cracks that cut through
317 both, sand grains and cement. This is observed in samples deformed at low
318 confining pressure (e.g., OR42, 800 MPa, Fig. 6a) and at higher confining pressure
319 (546LN, 1000 MPa, Fig. 6b). In samples deformed at low confining pressure, cracks
320 are subparallel to the loading direction and appear to have been dilatant, mode I
321 cracks, before new quartz material has filled the cracks. The inner parts of these
322 cracks can be filled with non-luminescent material (Fig. 6a). From the boundaries of
323 the healed mode I cracks, very thin cracks extend perpendicular to the mode I
324 cracks, i.e., in an orientation typical for unloading cracks (Fig. 6a). The appearance
325 of such cracks has first been observed in samples deformed in the Griggs-type
326 apparatus by Fitz Gerald et al. (1991), and these features have been termed "step-
327 ladder cracks". In all deformed samples, many thin cracks with bright luminescence
328 in a direction perpendicular to the shortening direction extend from grain boundaries
329 and cracked regions and have formed as unloading cracks during decompression of
330 the samples (e.g., Fig. 6b).

331 In samples deformed at higher confining pressure, cracks tend to be thinner, more
332 irregular, and are distributed more pervasively across the samples (Fig. 5e,f). They
333 often (but not necessarily) follow the grain boundaries (intergranular cracks). For all
334 the cracks in the samples, no or very little displacement has been observed along
335 the cracks.

336 The brightly luminescing material sometimes forms overgrowths with crystal faces
337 on pre-existing large grains or filling intergranular spaces (Fig. 6c,d). EBSD maps
338 performed on these areas indicate that these faceted overgrowths are in
339 crystallographic continuity with the parent grain. The faceted crystals can be
340 surrounded by non-luminescent material in pore spaces (Fig. 6c,d).

Larger regions of bright luminescent material consist of aggregates of many small new grains (Fig. 6d). Many of the small grains are brightly luminescent throughout but others have a darker luminescent core with a bright rim of variable thickness (Fig. 6d). Comparison between bright luminescent zones and the corresponding regions under crossed polarizers indicate that all of these regions consist of small grains, luminescing in blue, but not all luminescent regions consist of small grains. The amount of brightly luminescent material increases substantially with increasing strain (see also below). In a sample deformed to 74% strain (OR56) the original grains are strongly elongated and are embedded in a matrix of 30% luminescent material (Figs. 5f & 12).

3.3.2.2 Evolution of luminescent regions as a function of pressure and sample strain

For four samples (546LN, OR42, OR57 and OR56), SEM-CL longitudinal transects have been recorded from the top to the bottom (example for OR57 sample on Fig. 7). All transects were segmented manually in order to separate the original sand grains and cement from the bright luminescent material. The segmented images were then processed with the *ImageJ* software in order to quantify the amount of bright luminescence regions in samples.

Domains with higher finite strain show a higher proportion of brightly luminescent areas. This relationship can be observed at the scale of a given sample, between the top – relatively undeformed part – and the bottom part – where deformation is much more intense (OR62, Figs. 5e & 8a). The relationship can also be observed in samples deformed to different amounts of total strain (e.g, OR56; Fig. 5f). There is a relationship between the amount of brightly luminescent material and confining pressure demonstrated for the three samples strained up to 30% (OR42, 546LN and OR57). The amount of brightly luminescent material increases in the middle to

bottom part of the samples (more deformed regions; Fig. 8a): 9.88% for sample OR42 (800 MPa), 10.72% for sample 546LN (1000 MPa), 15.08% for sample OR57 (2000 MPa; Fig. 7). Thus, there is a trend of increasing amount of brightly luminescent material with increasing confining pressure and with strain (Fig. 8b).

3.4 Strain analysis from fabric and grain shapes

The starting material and samples deformed at 700, 1000, 1500 and 2000 MPa confining pressure have been studied for their grain shapes and fabric by image analysis. The goal of the analysis was to compare the bulk sample strain determined from the mechanical record and from measuring sample lengths with an analysis based on strain of individual quartz grains. Such an analysis is difficult in normal quartz grain aggregates because the regions of dynamic recrystallization make it difficult to identify original grain shapes as passive markers. The outlines of original sand grains in the Tana quartzite represent true strain markers for the deformed samples, because dynamic recrystallization typically affects the grain boundary region first (e.g. formation of “core and mantle” structures), i.e. the cement regions. However, the sand grain outlines are located inside the original quartz grains and are only rarely affected by the bright luminescence regions. Furthermore, they present passive markers because the cement overgrowth is in crystallographic continuity with the original sand grains. In addition, the orientation of long axes of the sand grains and their fabric are more or less random in the starting material (Table 1).

An example of the segmentation of the OR62 sample (2000 MPa) is shown in Fig. 9. Sand grains are manually separated from surrounding cement in LM-CL-images. In this way, only the original sand grains and their internal plastic deformation are considered for this strain analysis.

Sand grain size and parameters calculated from the analysis of mosaic LM

cathodoluminescence images are presented in Table 4. The number of analysed grains varies with the grain sizes (sample size for 546LN is smaller). The equivalent diameter of sand grains varies with the layers in the starting material and is not a function of deformation. The aspect ratio of individual grains increases for deformed samples (from 1.55 to 2.05) in comparison to the starting material. No correlation emerges between confining pressures and equivalent diameters or aspect ratios neither with sample bulk strain (calculated or measured).

The SURFOR program facilitates the calculation of the sample strain/fabric anisotropy from the particle outlines of the starting material and deformed samples. The results are presented in Table 5 and shown in Fig. 10. The difference between the minimum and maximum of the projection curves corresponds to the global strain value (from 0 to 1). The angular difference between the maximal and minimal position of the projection curve should be 90° (corresponds to the angle between shortening and extension direction), and the value of the minimum corresponds to the shortening direction.

For the starting material (TQ) the minimum of the curve is 0.965 for α=70°, indicating a very slight flattening of the grains. However, as the studied thin section was not oriented in a particular way and the cores for experimental samples were not made in the same orientation, this value indicates the general fabric anisotropy of the starting material but does not correspond to the orientation of this material in the apparatus. Yet, we should consider the ± 3.5 % anisotropy as a mean error for strained samples.

For deformed samples, the bulk shortening for the grain fabric calculated by the SURFOR analysis is between 22.9 and 37.2%. For the samples OR52, OR64 and OR62 the values are very close to the ones calculated from mechanical data and

417 measured on thin sections and are within the error range (± 3.5%). However, for
418 546LN, the shortening value is underestimated and overestimated for OR32
419 (difference up to > 8%).

420 *3.5 EBSD maps and misorientation calculations*

421 Two regions were selected for detailed EBSD analysis: (1) a low strain region with
422 limited recrystallization and formation of discrete luminescence in response to
423 cracking (546LN), and (2) a high strain region affected by more extensive
424 recrystallization/luminescent material (OR56).

425 In region (1) the cracks are visible in the SEM-CL image, cutting through original
426 quartz sand grains as well as cement (Fig. 11a). The corresponding EBSD map of
427 this region shows small new grains (clasts) that make high angle boundaries with the
428 larger quartz grains in the traces of the cracks. In addition, some low angle
429 boundaries also separate the small clasts from the host quartz grains (Fig. 11b). The
430 size of the clasts (new grains) can be as small as 1-2 μm and as large as ~10 μm
431 (Fig. 13). Low angle new grains (in Fig. 13 marked as “subgrains”) and the high
432 angle new grains (in Fig. 13 marked as “recrystallized grains”) do not show different
433 size distributions, only high angle new grains are more frequent (Fig. 13). On the
434 scale of the EBSD maps, the smaller and larger clasts all have more or less rounded
435 shape (Fig. 6c,d). This is the case in light microscope images, too (Fig. 4). The clasts
436 typically have a bright blue luminescence colour. The clasts with low angle
437 boundaries (< 10°) only show a weakly preferred misorientation axis in [0001],
438 whereas the larger angle boundaries are misoriented with axes in [0001] and [-12-10].

439 In the high strain region (2), the original quartz grains appear bright in the SEM-CL
440 image, and the recrystallized matrix is medium grey (blue luminescence; Fig. 12).
441 Some relict parts of original quartz grains are present as porphyroclasts with bright

luminescence surrounded by a matrix of recrystallized grains (separated mostly with high angle boundaries). The corresponding EBSD map shows a large number of recrystallized grains of 1-2 μm size with high angle boundaries in the matrix (Fig. 13). The two large relict quartz grains (labelled 1744 and 3542 in Fig. 12) show a number of subgrains with low angle boundaries (< 10° misorientation from the large quartz porphyroclast) forming regions of subgrains between the porphyroclast and the recrystallized matrix. The subgrains do not show different luminescence from their host grains. The two large grains show different distributions of misorientation axes for their subgrains: [0001] (in 1744) and no preferred axis (in 3542). The high angle grain boundary misorientations (Fig. 12c,d) have rotation axes of [1-100] (in 3542) and axes between [1-100] and [-12-10] (in 1744). The subgrain sizes are in the same range as the sizes of small recrystallized grains (Fig. 13).

The sizes of relict grains do not differ between the two microstructures (Fig. 13 and Table 6). Relict grains are those grains that are located in a matrix of recrystallized grains. The original large porphyroclasts of the starting material typically are too large to be included completely in the EBSD maps. They are cut off at the margins of the map and therefore are not counted. The proportion of subgrains and recrystallized grains is much higher in the high strain sample OR56 than in the lower strain sample 546LN (Fig. 13).

4. Discussion

4.1 Deformation processes

We observe two deformation processes that operate in all deformed samples: Cracking and crystal plastic deformation. Crystal plastic deformation is visually dominant in the microstructures, and the fact that the bulk sample strain can be calculated from the particle strain of original sand grains within a few percent error (Fig. 10, Tables 2 & 5) documents that most of the bulk shortening of the samples is

produced by crystal plastic deformation of individual original quartz grains. The undulatory extinction, deformation lamellae, and progressive subgrain rotation (Figs. 4 & 12) observed in the quartz grains are consistent with this observation. Thus, the dominant process of deformation in all samples is crystal plastic deformation, i.e. dislocation creep, as it has been documented previously for quartz under these P-, T-, strain rate conditions (e.g., Griggs, 1967; Jaoul et al., 1984; Kronenberg and Tullis, 1984; Hirth and Tullis, 1992).

Despite the dominance of plasticity, cracking takes place in all samples (Figs. 5 & 6). Even though the crack morphology changes with confining pressure, there is one feature that is common to all observed cracking: the cracks accommodate very little displacement, so that the cracks do not contribute significantly to the finite strain. Furthermore, the highest stresses attained in these experiments are all (except sample OR60) below the Goetze criterion ($\Delta\sigma < P_{conf}$). This criterion defines the upper differential stress limit of plastic or viscous deformation (brittle-plastic transition; Kohlstedt et al., 1995). In the presence of a pore fluid, this criterion has to be considered with some care (Hirth and Beeler, 2015; Beeler et al., 2015). The effect of pore pressure at high pressure and temperature conditions and small amounts of pore fluid is poorly investigated, but recent results by Okazaki et al. (2021) indicate that at the porosity of our experiments (0.12 vol%, using the density of H_2O from data by Larrieu and Ayers (1997)), the potentially expected reduction of differential stress by pore pressure effects should be in the range of experimental error (± 30 MPa; Holyoke and Kronenberg, 2010). Thus, the effective pressure coefficient α in $\sigma_{eff} = \sigma_n - \alpha P$ (see Beeler et al., 2015) should be close to zero, so that dominant viscous deformation can be concluded from the mechanical data for all of the samples, consistent with the dominant deformation mechanism in the microstructures.

494 The observed mode I cracks (Fig. 6a) have geometries typical of those formed at
495 low confining pressures (P_{conf}), (e.g. Paterson and Wong, 2005) and their occurrence
496 in samples deformed at the lowest P_{conf} is not surprising. We expect that such cracks
497 in the higher pressure samples have formed during early stages of the experiments,
498 by processes described previously in quartz experiments in the solid medium
499 apparatus (Fitz Gerald et al., 1991; Chernak et al., 2009; Tarantola et al., 2010;
500 Stünitz et al., 2017). These stepladder cracks (Fig. 6a,b) form as the result of a
501 sequence of initial cracking and subsequent crack healing, during which dislocations
502 are produced, followed by the glide of some of these dislocations. As a
503 consequence, there is a zone of plastically shortened material that forms
504 immediately adjacent to the crack. During unloading of the sample at the end of the
505 experiment this zone expands and develops unloading cracks (Fitz Gerald et al.,
506 1991; Stünitz et al., 2003, 2017). In this way the stepladder cracks document the
507 initiation of crystal plastic deformation in which local brittle processes and healing of
508 cracks play an important role. The CL observations document that cracking is a
509 ubiquitous feature during the dominant plastic deformation of quartz at high
510 temperatures of 900°C. At higher confining pressures cracks tend to have a different
511 geometry, but the interaction of cracking, crack healing, and plastic deformation is
512 not expected to change. The microstructures also document that cracking without
513 major displacement and thus without major kinematic contribution to strain
514 accommodation may be common at high temperatures when the sample strain is
515 dominantly accommodated by plastic mechanisms and flow stresses are low,
516 especially at high confining pressure (Fig. 2).

517 *4.2 Recrystallization processes*

518 Recrystallized material in all samples is marked by blue luminescence. The blue
519 luminescence colour is caused by a re-working (recrystallization) of quartz involving

520 an interaction with the aqueous fluid facilitating an exchange of trace elements or
521 producing defects during crystal growth (e.g. Ramseyer et al., 1988; Götze et al.,
522 2001). The blue luminescence is and has been attributed to Ti-incorporation into
523 quartz (Spear and Wark, 2009; Bestmann and Pennacchioni, 2015). It is unclear how
524 Ti-incorporation could have been achieved in the deformed samples in our
525 experiments, because a major Ti-source is lacking (although minute amounts of Ti-
526 phases (rutile) are present in the starting material) and Ti-incorporation during
527 recrystallization has been demonstrated to be slow and not producing homogeneous
528 equilibrium compositions easily (Negrini et al., 2014). A detailed analysis of the trace
529 element exchange that causes the luminescence was not attempted here because it
530 is beyond the scope of this study. However, as a potential origin of luminescence by
531 deformation-induced defects is very unlikely – these defects in quartz typically show
532 red luminescence colours (Hamers et al., 2016, 2017), and this type of luminescence
533 disappears after some electron beam irradiation (Bestmann, pers. Comm.) – it is
534 inferred that luminescence is caused by an interaction of the quartz with an aqueous
535 fluid during the reconstitution of the material. Therefore, it is concluded that the
536 luminescence observed in our samples is the result of exchange of trace elements
537 with a fluid during recrystallization of quartz (facilitated by boundary migration). This
538 makes luminescence a useful tool to trace recrystallized material in the deformed
539 samples.

540 Some of the recrystallization takes place by progressive subgrain rotation as
541 documented by EBSD maps (Figs. 11 & 12). Subgrains with misorientation angles of
542 < 10° are dominantly rotated around the [c]-axis. Such rotations can be produced by
543 tilt walls made up of edge dislocations in the prism planes with <a> Burgers vectors
544 or by twist boundaries in the basal plane made up of screw dislocations with <a>
545 Burgers vectors (e.g., Trépied et al., 1980; Kilian and Heilbronner, 2017). Thus, this

546 constitutes evidence for prism <a> or basal <a> slip. For misorientations > 10°,
547 rotation axes are parallel to [-1100] or between [-1100] and [-12-10], consistent with
548 basal <a> or combined basal <a> and prism <c> slip. However, it is difficult to infer
549 slip systems accurately for larger misorientation angles, because misorientations
550 may partially be produced by grain boundary sliding processes once high angle
551 boundaries are established. The microstructures of subgrain boundaries within
552 original quartz porphyroclasts and the immediately adjacent grains with high angle
553 boundaries exhibit core-mantle structures (Fig. 12) and indicate progressive subgrain
554 rotation as the dominant recrystallization mechanism for such grains. Subgrains with
555 low angle boundaries and recrystallized grains with high angle boundaries do not
556 differ systematically in size (Fig. 13). The P-, T-, strain rate conditions of deformation
557 of the samples are those of regime 2 creep according to Hirth and Tullis (1992),
558 where rotation recrystallization is dominant. In these microstructures, the
559 luminescence of the porphyroclasts and their subgrains does not change, so that
560 non-recrystallized parts of porphyroclasts with subgrains still maintain the original
561 luminescence of the porphyroclasts (Fig. 12a). This observation is consistent with the
562 process of fluid exchange discussed by Negrini et al. (2014): formation of subgrain
563 boundaries is a climb process, which does not *a priori* involve any grain boundary
564 mobility and thus no interaction or exchange with a fluid phase. Once high angle
565 boundaries are established, grain boundary mobility may lead to exchange with a
566 fluid, producing different luminescence colours of these recrystallized grains.

567 A completely different process can form new grains in the deformed samples, too.
568 Local cracking produces small new grains, especially at grain boundaries and in local
569 cracks cutting through original quartz grains (Figs. 5, 6 & 11). Some new grains show
570 high angle misorientation relationships, whereas others show low angle relationships
571 along the same zones of cracks (Fig. 11). The CL images indicate that in some

572 cases, inner parts of clasts can still show the original luminescence of old grains,
573 whereas rims and small grains nearby show the blue luminescence typical of
574 reconstituted material (Figs. 6d, 11, 16). From these microstructures, it is inferred
575 that the small clasts in cracks have mobile boundaries that migrate and can produce
576 a reconstitution (recrystallization) of the quartz and exchange trace elements to
577 produce the different luminescence. Local grain boundary migration processes have
578 been inferred in previous studies (Stipp et al., 2002a, 2002b), where the migration
579 process is inferred to be the first step. A second type of process is subsequently
580 required to produce isolated new grains, because the local migration itself cannot
581 isolate small new grains. This second step can be subgrain formation and/or local
582 cracking (Stipp et al., 2002a, 2002b). In this study, we can observe the dominance of
583 cracking in certain locations of the sample, where new grains form (Figs. 4 & 5). The
584 sequence in this study is reversed: the cracking occurs first, followed by boundary
585 migration to exchange with the fluid. It is proposed here that cracking and local
586 boundary migration operate to produce microstructures that are consistent with what
587 is termed “bulging recrystallization” in the literature (e.g., Bailey and Hirsch, 1962;
588 Stipp et al., 2002a, 2002b; Stipp and Kunze, 2008). Local bulging may occur in these
589 samples, too, so that probably not all of the bulging recrystallization microstructures
590 are induced by cracking.

591 The brittle origin of new grains in quartz and other silicates during plastic
592 deformation has been described by van Daalen et al. (1999) in natural rocks, and by
593 Stünitz et al. (2003, 2017) and Vernooij et al. (2006) in experiments. The CL-
594 microstructures of these deformed samples indicate that the original clasts become
595 modified by grain boundary migration processes after their initial formation by
596 cracking. The misorientation of the small clasts with low angle boundaries shows a
597 weak preference of c-axis rotation, whereas higher angle boundaries can be

misoriented by c-, a-, or m-axis rotation (Fig. 11).

Grains with blue luminescence and faceted crystal shapes in open pore spaces tend to show oriented overgrowth in crystallographic continuity with original porphyroclasts (Figs. 6c & 11b) and have been described by Palazzin et al. (2018) for dilatant sites that act as small local reservoirs of fluids. These microstructures testify to the fast precipitation in dilatant sites and to the fact that there is excess H_2O in these samples (so that $a_{H2O} = 1$). Thus, the samples deformed at different confining pressures show two types of recrystallization that takes place during deformation: (1) progressive subgrain rotation, and (2) crack-related local grain boundary migration that appears to be a type of bulging recrystallization. Both operate at the same time in samples, although the geometry of some cracks indicates an early origin of these.

4.3 Dislocation creep and stress exponent

From the conclusion of crystal plasticity, the operation of climb and dislocation glide are dominant deformation mechanisms, an n-value for the stress exponent of n = 3 to 5 would be expected for climb controlled creep (e.g., Paterson, 2012). Our strain rate stepping experiments have yielded n-values of ~1.4 or ~2, depending on whether the slowest strain rate steps are considered or not. The variance of these values and the uncertainty of the slowest strain rate steps require more detailed investigation and a better data base to determine the stress exponent more accurately. However, the present determination of n~2 suggests values of n < 3 and is consistent with observations of Fukuda et al. (2018) and Richter et al. (2018) in quartz aggregates. Both research groups have concluded a contribution of diffusion creep (including dissolution precipitation creep) to the viscous deformation of quartz. Richter et al. (2018) have observed weaker preferred orientation of quartz in fine grained aggregates, and the n~2 values are explained by a combination of

dislocation and diffusion creep deformation in their samples. The values obtained here are lower than n = 3 to 5, too, and therefore inconsistent with typical n-values for pure dislocation creep (Fig. 3b).

The starting material in the samples of this study is coarse grained, so that diffusion creep in the starting material is unlikely. However, some of the recrystallized material (in particular the cracked material in bulging-type microstructures) is fine grained, and some diffusion creep in the recrystallized material is conceivable. In addition, extensive exchange with aqueous fluid in the recrystallized material is observed in our samples, so that diffusive mass transfer processes are evident. Thus, it is inferred that the low n-values of n~2 in our samples may also be explained by a combination of dislocation and diffusion creep processes. A potential explanation of dislocation accommodated grain boundary sliding (disGBS), as it is inferred in olivine (e.g., Hansen et al., 2012) is unlikely, because it would require the whole material to consist of fine grain sizes.

As diffusion creep is grain size dependent, its contribution to the deformation process is expected to increase with an increase of fine grained material or decrease with grain growth. In most of our samples, steady state deformation is observed (Fig. 2), as it is typical for the dislocation creep regime 2 as defined by Hirth and Tullis (1992). This observation suggests that an increase of recrystallized material does not increase the contribution of diffusion creep. The reason for this may be that grain growth (= migration processes) of very small grains produced by cracking takes these grains out of the diffusion creep field (producing an equilibrium recrystallized grain size). Continued microcracking may produce new very small grains, which in turn may grow. These processes appear to be in a steady state to produce steady state deformation. However, it is premature to speculate further on this aspect, and more research is required to investigate the relationship between cracking and

650 recrystallization processes in more detail.

651 *4.4 Effect of H_2O and pressure*

652 The progressive lowering of the flow stress with increasing confining pressure in
653 our samples is consistent with the initial observations by Kronenberg and Tullis
654 (1984) and Mainprice and Paterson (1984). When the stresses (taken at 15%
655 shortening, where all samples reach more or less steady state flow stress) are
656 plotted as a function of the confining pressures, a power law relationship between
657 the flow stress and the confining pressure of the form $\sigma_{diff} = 505522\ P_c^{-1.113}\ MPa$ is
658 found (Fig. 14), similar to that of Kronenberg and Tullis (1984). However, in this
659 study, a coarse grained quartzite instead of fine grained novaculite was used (as in
660 Kronenberg and Tullis, 1984), confirming that the process of pressure-dependent
661 weakening in quartz is not dependent on grain size of the starting material.

662 Kohlstedt et al. (1995) proposed that the pressure dependence of the rheology
663 should be expressed as a fugacity term with exponent m in the quartz flow law. The
664 log-log plot of flow stresses vs. fugacity (Fig. 15) allows a fit of the r = m/n value,
665 which is -0.46 for our samples. The plot in Fig. 15 shows other data from the
666 literature together with our data, but the curve fit is only shown for data of this study.
667 The r = m/n value is similar to that of Post et al. (1996) (-0.47), Kronenberg and Tullis
668 (1984) (-0.5, as fitted by Post et al., 1996), Chernak et al. (2009) (-0.40), and of
669 Holyoke and Kronenberg (2013) (-0.63, for their quartzite). It should be noted that
670 experiments by Kronenberg and Tullis (1984) and Holyoke and Kronenberg (2013)
671 were performed at 800°C, those of Post et al. (1996) and Chernak et al. (2009) at
672 900°C and 1.5 GPa. A linear regression to all existing data yields almost the same
673 slope as our data (0.458 vs. 0.460), but with a much lower correlation coefficient
674 (0.71 vs. 0.93). This situation confirms the validity and applicability of our new data
675 set.

The exponent m for the fugacity depends on the n-value of the stress exponent. In this study, a stress exponent of n∼2 is inferred, which would result in an m-value of 0.92, or m∼1. An m-value of m=1 has been determined by Fukuda et al. (2018) for their n-value of 1.7, quite consistent with our results. If n-values closer to n=4 are chosen, as determined by Paterson and Luan (1990) and Gleason and Tullis (1995) and used in Hirth et al. (2001) and others, or n=2.7 (or n∼3, Rutter and Brodie, 2004), as proposed by Tokle et al. (2019), the m-value would be m=1.84 or 1.24. However, the original m-value of 1 proposed by Kohlstedt et al. (1995) is consistent with our results and those of Fukuda et al. (2018) for their m/n and n-values.

Lu and Jiang (2018) have proposed to correct the quartz flow law for pressure by using an activation volume term. This correction would have the opposite effect as the fugacity correction, and it is only meaningful to employ such a term once the activation energy is precisely determined. The presently existing data base of Q-values shows a large scatter (see compilation in, e.g., Richter et al., 2018), so that it appears to be necessary to determine Q accurately as a first step, before an activation volume term needs to be considered. We therefore do not consider the activation volume here.

4.5 What is the cause of sample weakening with increasing pressure?

In previous studies of quartz deformation with the presence of H_2O the weakening effect has been inferred as due to enhanced recrystallization or recovery (Tullis et al., 1979; Tullis and Yund, 1989). Subgrain boundary formation is enhanced in quartzites deformed with H_2O and grain boundary migration forms dislocation-free grains during dynamic recrystallization. Both processes are faster at higher confining pressures. Our results are consistent with this interpretation. The amount of recrystallized material increases with increasing confining pressure (Fig. 8), and this is the most obvious difference in the microstructures with increasing confining

pressure, apart from a different crack geometry. The recrystallization in our samples involves grain boundary migration, which, in the presence of an aqueous fluid, can be described as a process of solution and precipitation with a very short transport distance of dissolved species across the boundary region. The solubility of SiO_2 increases non-linearly with increasing pressure (e.g., Manning, 1994, 2018), so that enhanced boundary migration rates are likely with increasing pressure because of enhanced solubility of quartz, provided that an efficient precipitation process can be identified. The precipitation may be favoured at local dilatant sites which may form by grain boundary sliding and in which precipitation has been observed or inferred (Fusseis et al., 2009; Menegon et al., 2015; Okudaira et al., 2015; Précigout and Stünitz, 2016, Précigout et al., 2017, 2019). In fine grained material, grain boundary sliding is an important mechanism to accommodate shape changes of grains induced by plastic deformation of grains (glide of dislocations) and to adjust for the plastic strain incompatibilities as a consequence of an insufficient number of slip systems in silicates (compared to metals). The low n-values (Fig. 3) in strain rate stepping experiments are consistent with grain boundary sliding and diffusion creep components of deformation. Grain boundary sliding and local dilatancy in the form of cavitation is likely to occur in these aggregates and may cause immediate oversaturation of the fluid and precipitation of quartz. Overgrowth of quartz seams on quartz grains is observed in larger dilatant sites (Fig. 6c). Replacement of quartz material during grain boundary migration is evident from the change of CL colours in the recrystallized material, indicating boundary migration by dissolution, precipitation, and exchange of elements with a fluid.

It has been pointed out above that once high angle boundaries are established, the distinction of grains formed by progressive subgrain rotation and those produced from initial cracking is possible (Pongrac et al., in prep.), but it is not easy, because

their size is similar and they all show bright luminescence. It is inferred that in this material the weakening effect takes place as a consequence of increased confining pressure. The inference that the pressure-dependent H_2O-weakening is caused by grain boundary processes is supported by the observation by Holyoke and Kronenberg (2013) that the pressure dependence of the flow stress in polycrystalline aggregates is greater than in single crystals. Consequently, these authors have attributed the weakening effect to recrystallization/recovery processes (Tullis and Yund, 1989) at grain boundaries, too.

The plot in Fig. 15 suggests that the pressure effect of H_2O-weakening could be greater at low pressure than at high pressures. A potentially greater m-value may be caused by a change in n- or r-values in m = r/n. The determination of the stress exponent is not precise enough at this stage to decide whether a constant n-value would require an intrinsic effect of the H_2O fugacity or whether the potentially changing pressure dependence of flow stress could be caused by a change in the stress exponent n.

4.6 Geological application

The lowering of quartz flow stresses with increasing confining pressures that has been documented since the study by Kronenberg and Tullis (1984) – also documented in this study – suggests that in subduction channels at high pressure the strength of quartz dominated lithologies is expected to be very low. Low stresses for deformation in subduction zones have been inferred by Stöckhert et al. (1997, 1999), Stöckhert and Renner (1998), Stöckhert (2002) and Wassmann and Stöckhert (2013), partly based on different deformation mechanisms. This study confirms that even for dislocation creep, where stresses tend to be higher than for diffusion creep, flow is expected to take place at very low stresses at high confining pressures of 2 GPa and higher.

754 The recrystallization mechanism of bulging recrystallization in quartz is usually
755 observed at low temperature conditions or the onset of crystal plastic deformation
756 (e.g., Stipp et al., 2002a, 2002b). The interaction of cracking and local grain
757 boundary migration indicates that some new grains in this recrystallization process
758 can be generated by cracking. One consequence of this process is that the host
759 control in new grain nucleation will be more difficult to determine, because small
760 rotation of new grains is likely, (e.g., van Daalen et al., 1999), but the rotation sense
761 and misorientation relationship is not necessarily clear and is not dependent on slip
762 systems.

763 Cracks are abundant in high pressure samples deformed by plastic mechanisms
764 at high temperature, in spite of the low deviatoric stress (~100 MPa) and the high
765 normal stress acting on any potential fracture plane (P_C ~2 GPa) – there is no or
766 very little displacement on these cracks. The interaction of cracking, crack healing,
767 and plasticity has been shown by Fitz Gerald et al. (1991) and Stünitz et al. (2017).
768 These observations suggest that in natural rocks, microcracks may play an important
769 role in the initiation of plastic deformation and during dynamic recrystallization, even
770 for the deep levels of the crust where high temperatures enable viscous deformation
771 at low deviatoric stresses.

772 **5. Conclusions**

773 The deformation of quartzites in the presence of 0.1 wt.% of added H_2O shows
774 decreasing flow stresses with increasing confining pressure. An r-value of 0.46 can
775 be fitted to the fugacity data, resulting in an m-value of ~1 for the fugacity coefficient
776 at an n-value of ~2. In addition, the following observations have been made:

777 1. The dominant deformation process is crystal plasticity in original quartz grains,
778 so that the strain analysis of quartz grains matches the bulk sample strain with an

779 error of a few percent. Dynamic recrystallization and recovery processes are
780 observed, too, so that the dominant deformation mechanism is dislocation creep.
781 Some cracking occurs during plastic deformation, but as the cracks do not display
782 significant offset, their contribution to the bulk strain is negligible.

783 2. Dynamic recrystallization of the deforming quartz grains takes place by
784 progressive subgrain rotation and by local grain boundary migration. The grain
785 boundary migration affects small clasts produced by cracking as well as former
786 subgrains once high angle boundaries have been established. The recrystallized
787 material acquires a different luminescence colour (blue), which can be used to track
788 the recrystallized material in the microstructures. The processes indicate that
789 nucleation of new grains may take place by cracking (in addition to other processes)
790 and appears to be an important part of a process that is termed “bulging
791 recrystallization”.

792 3. The stress exponent n is approximately equal to 2, when some diffusive mass
793 transfer is important during dislocation creep. This contribution is likely to be fluid-
794 dependent or fluid enhanced.

795 4. The amount of recrystallized material increases with increasing confining
796 pressure. It is inferred that the increasing confining pressure has an enhancing effect
797 on the grain boundary migration rate and thus recrystallization rate.

798 **Acknowledgements**

799 We thank Rune Stien (ELKEM) and Raoul Heilbronner for their help with the
800 sampling of the quartzite at Austertana. We thank Ida Di Carlo for her support with
801 SEM-cathodoluminescence, Aneta Slodczyk for her precious help with FTIR
802 measurements, and Audrey Sauldubois for TEM support. We thank Greg Hirth and
803 Andreas Kronenberg for their very insightful and constructive reviews. P. Pongrac

acknowledges support from the grant agency of Charles University (GAUK 488119) and the Centre of Geosphere Dynamics (UNCE/SCI/006).

Support from the VOLTAIRE (ANR-10-LABX-100-01) and PLANEX (ANR-11-EQPX-36) projects funded by ANR through the PIA (Programme d'Investissement d'Avenir) is gratefully acknowledged.

References

Aasly, K., Malvik, T., Myrhaug, E.H., 2007. Advanced methods to characterize thermal properties of quartz. Conf. Paper INFACON 11, Innovations in Ferro Alloy Industry, http://citeseerx.ist.psu.edu/viewdoc/download?doi=10.1.1.607.1094&rep=rep1&type=pdf

Bachmann, F., Hielscher, R., Schaeben, H., 2011. Grain detection from 2d and 3d EBSD data—Specification of the MTEX algorithm. Ultramicroscopy 111, 1720–1733. https://doi.org/10.1016/j.ultramic.2011.08.002

Bailey, J.E., Hirsch, P.B., 1962. The recrystallization process in some polycrystalline metals. Proc. Royal Soc. London, A 267, 11-30.

Beeler, N.M., Hirth, G., Thomas, A., Bürgmann, R., 2016. Effective stress, friction, and deep crustal faulting. Journal of Geophysical Research: Solid Earth 121, 1040–1059. https://doi.org/10.1002/2015JB012115

Bestmann, M., Pennacchioni, G., 2015. Ti distribution in quartz across a heterogeneous shear zone within a granodiorite: The effect of deformation mechanism and strain on Ti resetting. Lithos 227, 37–56. https://doi.org/10.1016/j.lithos.2015.03.009

Blacic, J.D., 1981. Water diffusion in quartz at high pressure: Tectonic implications. Geophysical Research Letters 8, 721–723. https://doi.org/10.1029/GL008i007p00721

Bunge, H.J., 1982. Texture analysis in materials science–mathematical methods. Lst Edn 2–35.

Chernak, L.J., Hirth, G., Selverstone, J., Tullis, J., 2009. Effect of aqueous and carbonic fluids on the dislocation creep strength of quartz. Journal of Geophysical Research: Solid Earth 114. https://doi.org/10.1029/2008JB005884

Fitz Gerald, J.D., Boland, J.N., McLaren, A.C., Ord, A., Hobbs, B.E., 1991. Microstructures in water-weakened single crystals of quartz. Journal of Geophysical Research 96, 2139. https://doi.org/10.1029/90JB02190

Fukuda, J., Holyoke, C.W., Kronenberg, A.K., 2018. Deformation of Fine-Grained Quartz Aggregates by Mixed Diffusion and Dislocation Creep. Journal of Geophysical Research: Solid Earth 123, 4676–4696. https://doi.org/10.1029/2017JB015133

Fusseis, F., Regenauer-Lieb, K., Liu, J., Hough, R.M., De Carlo, F., 2009. Creep cavitation can establish a dynamic granular fluid pump in ductile shear zones. Nature 459, 974–977. https://doi.org/10.1038/nature08051

Gerretsen, J., Paterson, M.S., McLaren, A.C., 1989. The uptake and solubility of water in quartz at elevated pressure and temperature. Physics and Chemistry of Minerals 16. https://doi.org/10.1007/BF00199553

Gleason, G.C., Tullis, J., 1995. A flow law for dislocation creep of quartz aggregates determined with the molten salt cell. Tectonophysics 247, 1-23

Götze, J., Plötze, M., Habermann, D., 2001. Origin, spectral characteristics and practical applications of the cathodoluminescence (CL) of quartz - a review. Mineralogy and Petrology 71, 225–250. https://doi.org/10.1007/s007100170040

Griggs, D.T., Blacic, J.D., 1965. Quartz: Anomalous Weakness of Synthetic Crystals. Science 147, 292–295. https://doi.org/10.1126/science.147.3655.292

857 Griggs, D., 1967. Hydrolytic Weakening of Quartz and Other Silicates*. Geophysical
858 Journal of the Royal Astronomical Society 14, 19–31.
859 https://doi.org/10.1111/j.1365-246X.1967.tb06218.x
860 Hamers, M.F., Pennock, G.M., Herwegh, M., Drury, M.R., 2016. Distinction between
861 amorphous and healed planar deformation features in shocked quartz using
862 composite color scanning electron microscope cathodoluminescence (SEM-
863 CL) imaging. Meteoritics & Planetary Science 51, 1914–1931.
864 https://doi.org/10.1111/maps.12711
865 Hamers, M.F., Pennock, G.M., Drury, M.R., 2017. Scanning electron microscope
866 cathodoluminescence imaging of subgrain boundaries, twins and planar
867 deformation features in quartz. Physics and Chemistry of Minerals 44, 263–
868 275.
869 Hansen, L.N., Zimmerman, M.E., Kohlstedt, D.L., 2012. The influence of
870 microstructure on deformation of olivine in the grain-boundary sliding regime.
871 Journal of Geophysical Research: Solid Earth 117.
872 https://doi.org/10.1029/2012JB009305
873 Heilbronner, R., 2002. Analysis of bulk fabrics and microstructure variations using
874 tesselations of autocorrelation functions. Computers & Geosciences 28, 447–
875 455. https://doi.org/10.1016/S0098-3004(01)00088-7
876 Heilbronner, R., Tullis, J., 2002. The effect of static annealing on microstructures and
877 crystallographic preferred orientations of quartzites experimentally deformed
878 in axial compression and shear. Geological Society, London, Special
879 Publications 200, 191–218. https://doi.org/10.1144/GSL.SP.2001.200.01.12
880 Heilbronner, R., Barrett, S., 2013. Image Analysis in Earth Sciences: Microstructures
881 and Textures of Earth Materials. Springer, 520 pp., Heidelberg.

882 Hirth, G., Tullis, J., 1992. Dislocation creep regimes in quartz aggregates. Journal of
883 Structural Geology 14, 145–159. https://doi.org/10.1016/0191-
884 8141(92)90053-Y
885 Hirth, G., Teyssier, C., Dunlap, J.W., 2001. An evaluation of quartzite flow laws
886 based on comparisons between experimentally and naturally deformed rocks.
887 International Journal of Earth Sciences 90, 77–87.
888 https://doi.org/10.1007/s005310000152
889 Hirth, G., Beeler, N.M., 2015. The role of fluid pressure on frictional behavior at the
890 base of the seismogenic zone. Geology 43, 223–226.
891 https://doi.org/10.1130/G36361.1
892 Holyoke, C.W., Kronenberg, A.K., 2010. Accurate differential stress measurement
893 using the molten salt cell and solid salt assemblies in the Griggs apparatus
894 with applications to strength, piezometers and rheology. Tectonophysics 494,
895 17–31. https://doi.org/10.1016/j.tecto.2010.08.001
896 Holyoke, C.W., Kronenberg, A.K., 2013. Reversible water weakening of quartz. Earth
897 and Planetary Science Letters 374, 185–190.
898 https://doi.org/10.1016/j.epsl.2013.05.039
899 Jaoul, O., Tullis, J., Kronenberg, A., 1984. The effect of varying water contents on
900 the creep behavior of Heavitree quartzite. Journal of Geophysical Research:
901 Solid Earth 89, 4298–4312. https://doi.org/10.1029/JB089iB06p04298
902 Kilian, R., Heilbronner, R., 2017. Analysis of crystallographic preferred orientations of
903 experimentally deformed Black Hills Quartzite. Solid Earth 8, 1095.
904 Kohlstedt, D.L., Evans, B., Mackwell, S.J., 1995. Strength of the lithosphere:
905 Constraints imposed by laboratory experiments. Journal of Geophysical
906 Research: Solid Earth 100, 17587–17602.
907 Kronenberg, A.K., Tullis, J., 1984. Flow strengths of quartz aggregates: Grain size
908 and pressure effects due to hydrolytic weakening. Journal of Geophysical

909 Research: Solid Earth 4281–4297.
910 https://doi.org/10.1029/JB089iB06p04281@10.1002/(ISSN)2169-
911 9356.CHEMDEF1
912 Kronenberg, A.K., Kirby, S.H., Aines, R.D., Rossman, G.R., 1986. Solubility and
913 diffusional uptake of hydrogen in quartz at high water pressures: Implications
914 for hydrolytic weakening. Journal of Geophysical Research: Solid Earth 91,
915 12723–12741. https://doi.org/10.1029/JB091iB12p12723
916 Larrieu, T.L., Ayers, J.C., 1997. Measurements of the pressure-volume-temperature
917 properties of fluids to 20 kbar and 1000°C: A new approach demonstrated on
918 H2O. Geochimica et Cosmochimica Acta 61, 3121–3134.
919 https://doi.org/10.1016/S0016-7037(97)00155-5
920 Lu, L.X., Jiang, D., 2019. Quartz Flow Law Revisited: The Significance of Pressure
921 Dependence of the Activation Enthalpy. Journal of Geophysical Research:
922 Solid Earth 124, 241–256. https://doi.org/10.1029/2018JB016226
923 Luan, F.C., Paterson, M.S., 1992. Preparation and deformation of synthetic
924 aggregates of quartz. Journal of Geophysical Research: Solid Earth 97, 301–
925 320. https://doi.org/10.1029/91JB01748
926 Mainprice, D.H., Paterson, M.S., 1984. Experimental studies of the role of water in
927 the plasticity of quartzites. Journal of Geophysical Research: Solid Earth 89,
928 4257–4269. https://doi.org/10.1029/JB089iB06p04257
929 Manning, C.E., 1994. The solubility of quartz in H2O in the lower crust and upper
930 mantle. Geochimica et Cosmochimica Acta 58, 4831–4839.
931 https://doi.org/10.1016/0016-7037(94)90214-3
932 Manning, C.E., 2018. Fluids of the deep crust: Deep is different. Ann. Rev. Earth
933 Plan. Sci. 46, 67-97. https://doi.org/10.1146/annurev-earth-060614-105224
934 McLaren, A.C., 2005. Transmission Electron Microscopy of Minerals and Rocks.
935 Cambridge University Press.

936 Menegon, L., Fusseis, F., Stünitz, H., Xiao, X., 2015. Creep cavitation bands control
937 porosity and fluid flow in lower crustal shear zones. Geology 43, 227–230.
938 https://doi.org/10.1130/G36307.1
939 Negrini, M., Stunitz, H., Berger, A., Morales, L.F., 2014. The effect of deformation on
940 the TitaniQ geothermobarometer: an experimental study. Contributions to
941 Mineralogy and Petrology 167, 982.
942 Okazaki, K., Burdette, E., Hirth, G., 2021. Rheology of the Fluid Oversaturated Fault
943 Zones at the Brittle-Plastic Transition. Journal of Geophysical Research: Solid
944 Earth 126, e2020JB020804. https://doi.org/10.1029/2020JB020804
945 Okudaira, T., Jeřábek, P., Stünitz, H., Fusseis, F., 2015. High-temperature fracturing
946 and subsequent grain-size-sensitive creep in lower crustal gabbros: Evidence
947 for coseismic loading followed by creep during decaying stress in the lower
948 crust? Journal of Geophysical Research: Solid Earth 120, 3119–3141.
949 https://doi.org/10.1002/2014JB011708
950 Palazzin, G., Raimbourg, H., Stünitz, H., Heilbronner, R., Neufeld, K., Précigout, J.,
951 2018. Evolution in H2O contents during deformation of polycrystalline quartz:
952 An experimental study. Journal of Structural Geology 114, 95–110.
953 https://doi.org/10.1016/j.jsg.2018.05.021
954 Panozzo, R., 1984. Two-dimensional strain from the orientation of lines in a plane.
955 Journal of Structural Geology, Planar and Linear Fabrics of Deformed Rocks
956 6, 215–221. https://doi.org/10.1016/0191-8141(84)90098-1
957 Paterson, M., Kekulawala, K.R.S.S., 1979. The role of water in quartz deformation [+
958 Discussions]. Bulletin de Minéralogie 102, 92–100.
959 https://doi.org/10.3406/bulmi.1979.7261
960 Paterson, M., 1982. The determination of hydroxyl by infrared absorption in quartz,
961 silicate glasses and similar materials. Bulletin de Minéralogie 105, 20–29.
962 https://doi.org/10.3406/bulmi.1982.7582

963 Paterson, M.S., Luan, F.C., 1990. Quartzite rheology under geological conditions.
964 Geological Society, London, Special Publications 54, 299–307.
965 https://doi.org/10.1144/GSL.SP.1990.054.01.26
966 Paterson, M.S., Wong, T. (Eds.), 2005. Evolution of Physical Properties during Brittle
967 Failure. Experimental Rock Deformation — The Brittle Field. Springer, Berlin,
968 Heidelberg, 59–114. https://doi.org/10.1007/3-540-26339-X_5
969 Paterson, M.S., 2012. Materials Science for Structural Geology. Springer Science &
970 Business Media.
971 Pec, M., Stünitz, H., Heilbronner, R., Drury, M., 2016. Semi-brittle flow of granitoid
972 fault rocks in experiments. Journal of Geophysical Research: Solid Earth 121,
973 1677–1705. https://doi.org/10.1002/2015JB012513
974 Pevik, J.A., 2015. Geological and Mineralogical Characterization of the Upper Part of
975 the Gamasfjell Quartzite at the Vaggecearu Mountain. MSc thesis, 132 pp.,
976 NTNU Trondheim
977 Pitzer, K.S., Sterner, S.M., 1994. Equations of state valid continuously from zero to
978 extreme pressures for H2O and CO2. The Journal of Chemical Physics 101,
979 3111–3116.
980 Post, A.D., Tullis, J., Yund, R.A., 1996. Effects of chemical environment on
981 dislocation creep of quartzite. Journal of Geophysical Research: Solid Earth
982 101, 22143–22155. https://doi.org/10.1029/96JB01926
983 Précigout, J., Stünitz, H., 2016. Evidence of phase nucleation during olivine diffusion
984 creep: A new perspective for mantle strain localisation. Earth and Planetary
985 Science Letters 455, 94–105. https://doi.org/10.1016/j.epsl.2016.09.029
986 Précigout, J., Prigent, C., Palasse, L., Pochon, A., 2017. Water pumping in mantle
987 shear zones. Nature Communications 8, 15736.
988 https://doi.org/10.1038/ncomms15736

989 Précigout, J., Stünitz, H., Pinquier, Y., Champallier, R., Schubnel, A., 2018. High-
990 pressure, High-temperature Deformation Experiment Using the New
991 Generation Griggs-type Apparatus. JoVE (Journal of Visualized Experiments)
992 e56841. https://doi.org/10.3791/56841
993 Précigout, J., Stünitz, H., Villeneuve, J., 2019. Excess water storage induced by
994 viscous strain localization during high-pressure shear experiment. Scientific
995 Reports 9, 3463. https://doi.org/10.1038/s41598-019-40020-y
996 Ramseyer, K., Baumann, J., Matter, A., Mullis, J., 1988. Cathodoluminescence
997 Colours of α-Quartz. Mineralogical Magazine 52, 669–677.
998 https://doi.org/10.1180/minmag.1988.052.368.11
999 Richter, B., Stünitz, H., Heilbronner, R., 2018. The brittle-to-viscous transition in
1000 polycrystalline quartz: An experimental study. Journal of Structural Geology
1001 114, 1–21. https://doi.org/10.1016/j.jsg.2018.06.005
1002 Rutter, E.H., Brodie, K.H., 2004a. Experimental intracrystalline plastic flow in hot-
1003 pressed synthetic quartzite prepared from Brazilian quartz crystals. Journal of
1004 Structural Geology 26, 259–270. https://doi.org/10.1016/S0191-
1005 8141(03)00096-8
1006 Rutter, E. H., Brodie, K.H., 2004b. Experimental grain size-sensitive flow of hot-
1007 pressed Brazilian quartz aggregates. Journal of Structural Geology 26, 2011–
1008 2023. https://doi.org/10.1016/j.jsg.2004.04.006
1009 Skemer, P., Katayama, I., Jiang, Z., Karato, S., 2005. The misorientation index:
1010 Development of a new method for calculating the strength of lattice-preferred
1011 orientation. Tectonophysics 411, 157–167.
1012 https://doi.org/10.1016/j.tecto.2005.08.023
1013 Spear, F.S., Wark, D.A., 2009. Cathodoluminescence imaging and titanium
1014 thermometry in metamorphic quartz. Journal of Metamorphic Geology 27,
1015 187–205. https://doi.org/10.1111/j.1525-1314.2009.00813.x

1016 Stipp, M., Stünitz, H., Heilbronner, R., Schmid, S.M., 2002a. The eastern Tonale fault
1017 zone: a 'natural laboratory' for crystal plastic deformation of quartz over a
1018 temperature range from 250 to 700°C. Journal of Structural Geology 24,
1019 1861–1884. https://doi.org/10.1016/S0191-8141(02)00035-4
1020 Stipp, M., Stünitz, H., Heilbronner, R., Schmid, S.M., 2002b. Dynamic
1021 recrystallization of quartz: correlation between natural and experimental
1022 conditions. Geological Society, London, Special Publications 200, 171–190.
1023 https://doi.org/10.1144/GSL.SP.2001.200.01.11
1024 Stipp, M., Kunze, K., 2008. Dynamic recrystallization near the brittle-plastic transition
1025 in naturally and experimentally deformed quartz aggregates. Tectonophysics
1026 448, 77–97. https://doi.org/10.1016/j.tecto.2007.11.041
1027 Stöckhert, B., Massonne, H.-J., Ursula Nowlan, E., 1997. Low differential stress
1028 during high-pressure metamorphism: The microstructural record of a
1029 metapelite from the Eclogite Zone, Tauern Window, Eastern Alps. Lithos 41,
1030 103–118. https://doi.org/10.1016/S0024-4937(97)82007-5
1031 Stöckhert, B., Renner, J., 1998. Rheology of Crustal Rocks at Ultrahigh Pressure. In:
1032 Hacker, B.R., Liou, J.G. (Eds.), When Continents Collide: Geodynamics and
1033 Geochemistry of Ultrahigh-Pressure Rocks, Petrology and Structural Geology.
1034 Springer Netherlands, Dordrecht, 57–95. https://doi.org/10.1007/978-94-015-
1035 9050-1_3
1036 Stöckhert, B., Wachmann, M., Küster, M., Bimmermann, S., 1999. Low effective
1037 viscosity during high pressure metamorphism due to dissolution precipitation
1038 creep: the record of HP–LT metamorphic carbonates and siliciclastic rocks
1039 from Crete. Tectonophysics 303, 299–319. https://doi.org/10.1016/S0040-
1040 1951(98)00262-5

1041 Stöckhert, B., 2002. Stress and deformation in subduction zones: insight from the
1042 record of exhumed metamorphic rocks. Geological Society, London, Special
1043 Publications 200, 255–274.
1044 Stünitz, H., Fitz Gerald, J.D., Tullis, J., 2003. Dislocation generation, slip systems,
1045 and dynamic recrystallization in experimentally deformed plagioclase single
1046 crystals. Tectonophysics 372, 215–233. https://doi.org/10.1016/S0040-
1047 1951(03)00241-5
1048 Stünitz, H., Thust, A., Heilbronner, R., Behrens, H., Kilian, R., Tarantola, A., Gerald,
1049 J.D.F., 2017. Water redistribution in experimentally deformed natural milky
1050 quartz single crystals—Implications for H2O-weakening processes. Journal of
1051 Geophysical Research: Solid Earth 122, 866–894.
1052 https://doi.org/10.1002/2016JB013533
1053 Tarantola, A., Diamond, L.W., Stünitz, H., 2010. Modification of fluid inclusions in
1054 quartz by deviatoric stress I: experimentally induced changes in inclusion
1055 shapes and microstructures. Contributions to Mineralogy and Petrology 160,
1056 825–843. https://doi.org/10.1007/s00410-010-0509-z
1057 Tarantola, A., Diamond, L.W., Stünitz, H., 2010. Modification of fluid inclusions in
1058 quartz by deviatoric stress I: experimentally induced changes in inclusion
1059 shapes and microstructures. Contributions to Mineralogy and Petrology 160,
1060 825–843. https://doi.org/10.1007/s00410-010-0509-z
1061 Tokle, L., Hirth, G., Behr, W.M., 2019. Flow laws and fabric transitions in wet
1062 quartzite. Earth and Planetary Science Letters 505, 152–161.
1063 https://doi.org/10.1016/j.epsl.2018.10.017
1064 Trépied, L., Doukhan, J.C., Paquet, J., 1980. Subgrain boundaries in quartz
1065 theoretical analysis and microscopic observations. Physics and Chemistry of
1066 Minerals 5, 201–218.

1067 Tullis, J., Shelton, G.L., Yund, R.A., 1979. Pressure dependence of rock strength :
1068 implications for hydrolytic weakening. Bulletin de Minéralogie 102, 110–114.
1069 https://doi.org/10.3406/bulmi.1979.7263
1070 Tullis, J., Yund, R.A., 1989. Hydrolytic weakening of quartz aggregates: The effects
1071 of water and pressure on recovery. Geophysical Research Letters 16, 1343–
1072 1346. https://doi.org/10.1029/GL016i011p01343
1073 van Daalen, M., Heilbronner, R., Kunze, K., 1999. Orientation analysis of localized
1074 shear deformation in quartz fibres at the brittle–ductile transition.
1075 Tectonophysics 303, 83–107. https://doi.org/10.1016/S0040-1951(98)00264-9
1076 Vernooij, M.G.C., den Brok, B., Kunze, K., 2006. Development of crystallographic
1077 preferred orientations by nucleation and growth of new grains in
1078 experimentally deformed quartz single crystals. Tectonophysics, Deformation
1079 Mechanisms, Microstructure and Rheology of Rocks in Nature and
1080 Experiment 427, 35–53. https://doi.org/10.1016/j.tecto.2006.06.008
1081 Wassmann, S., Stöckhert, B., 2013. Low stress deformation of garnet by incongruent
1082 dissolution precipitation creep. Journal of Structural Geology 46, 200–219.
1083 https://doi.org/10.1016/j.jsg.2012.09.002

1084 **Figures and Tables**

1085 Figure 1. (a) Cross-polarized microphotograph of starting material Tana quartzite
1086 showing equant grains without undulatory extinction. (b) Pole figure of random
1087 crystallographic orientation of c-axis from 500 grains measured by EBSD. (c & d)
1088 Plane polarized light microscope-cathodoluminescence images: equant and rounded
1089 sand grains of various tints are surrounded by darker cement that grows in
1090 crystallographic continuity (arrows).

1091 Figure 2. Mechanical data for samples deformed in wet conditions (0.1 wt.% H_2O
1092 added) at 900°C for confining pressures between 600 and 2000 MPa. Samples …LN

have been deformed in Tromsø (Norway) whereas samples OR… have been deformed in Orléans (France). The samples strengths systematically decrease with increasing confining pressure.

Figure 3. (a) Stress strain curves obtained for strain rate stepping experiments at 800 MPa (OR79) and 2000 MPa (OR68). (b) Plot of the log strain rate vs. log flow stress. Solid circles are data obtained from strain rate stepping experiments whereas open circles are data from samples deformed at 10^{-6} s^{-1} constant strain rate at the same confining pressures. The slopes of the regressed lines indicate n-values of ~1.40 at 2000 MPa and ~1.42 at 800 MPa.

Figure 4. Cross polarized light images of sample OR32 deformed at 1000 MPa confining pressure. Left: overview of sample showing higher strain regions near the centre of the sample. In the most strongly deformed part of the sample, clasts are elongated, and limited recrystallization is observed at grain boundaries (core-mantle structures). Right: details of the recrystallized region showing undulatory extinction, subgrains, and new grains. The shortening direction is vertical.

Figure 5. SEM-cathodoluminescence images of (a) starting material and of samples deformed at confining pressure of (b) 700 MPa (OR52), (c) 1000 MPa (546LN), (d) 1500 MPa (OR64), (e) 2000 MPa (OR62) and (f) 2000 MPa high-strain (74%; OR56). The shortening direction is vertical for images (b-f).

Figure 6. (a & b) SEM-CL-images of cracks in both cement and grains in sample deformed at (a) 800 (OR42) and (b) 1000 MPa (546LN) confining pressure. (c) Crystal faces at open grain boundary region in 546LN sample (1000 MPa). (d) Crystal faces in small luminescent grains in open space between grains in OR64 sample (1500 MPa). The shortening direction is vertical for all images.

1117 Figure 7. Left: mosaic of OR57 sample (2000 MPa) in polarized light with associated
1118 SEM-CL-images longitudinal transect. Right: examples of segmentation and
1119 identification of bright luminescent zones (coloured in blue).

1120 Figure 8. Percentage of bright luminescence for SEM-CL images longitudinal
1121 transects, (a) as a function of the position along the sample and (b) as a function of
1122 the confining pressure.

1123 Figure 9. Example of the manual segmentation made for the OR62 (2000 MPa) thin
1124 section from optical cathodoluminescence images. Interiors of grains are isolated
1125 from the surrounding cement based on their luminescence colour contrasts. The
1126 shortening direction is vertical.

1127 Figure 10. SURFOR projections curves showing that the starting material TQ2 has a
1128 slight strain of 3.5% whereas deformed samples at various confining pressures have
1129 an orientation comprise between 80 and 90° for a strain comprise between 24.6%
1130 (546LN) and 34.4% (OR52). The global shortening direction for deformed samples is
1131 theoretically 90°.

1132 Figure 11. Cathodoluminescence (CL) image, EBSD orientation map and inverse
1133 pole figures (IPF) for sample 546LN. (a) CL image with blue (380-515 nm) optical
1134 filter to highlight recrystallized areas; (b) EBSD map of quartz orientations coloured
1135 parallel to the X direction, sample is plotted with hexagonal symmetry (6/mmm) to
1136 account for the effect of Dauphiné twins. Grain boundaries are identified by black
1137 bounding lines and subgrains are identified by white boundaries. (c) IPF's for
1138 subgrain (defined by a misorientation between 2 and 10°) boundaries and (d) grain
1139 (defined by a misorientation greater than 10°) boundaries. All IPF's are plotted in
1140 hexagonal 6/mmm symmetry with the same scale for multiples of uniform (m.u.d.) for
1141 each plot. (e) Colour key for IPF ∥ X map.

1142 Figure 12. Cathodoluminescence (CL) image, EBSD orientation map, misorientation
1143 map and inverse pole figures (IPF) for high strain sample OR56. (a) CL image with
1144 blue (380-515 nm) filter to highlight recrystallized areas. (b) EBSD map of quartz
1145 orientations coloured parallel to the X direction, sample is plotted with hexagonal
1146 symmetry (6/mmm) to account for the effects of Dauphiné twins. Grain boundaries
1147 are identified by black bounding lines and subgrains are identified by white
1148 boundaries (see detailed insert at the top right hand corner). (c) Misorientation map
1149 where blue shows low misorientation and yellow shows high misorientation relative
1150 to the mean grain orientation. Grains 1744 and 3542 are highlighted on the IPF (bold
1151 black) and misorientation (red) maps. (d-f) IPF's for subgrain (defined by a
1152 misorientation between 2 and 10°) and grain (defined by a misorientation greater
1153 than 10°) boundaries with the d) full map, (e) grain 1744 and (f) grain 3542. All IPF's
1154 are plotted in hexagonal 6/mmm symmetry with the same scale for multiples of
1155 uniform distribution (m.u.d.) for each plot.

1156 Figure 13. Log_{10} grain size distributions for samples (a) 546LN and (b) OR56. Grain
1157 size distributions are separated into relict, recrystallized and subgrain populations.

1158 Figure 14. A power-law relationship fitted to the flow stresses (at 15% strain) at
1159 different confining pressures.

1160 Figure 15. Relationship between water fugacity and flow stresses. The slope
1161 indicates a m/n coefficient of 0.46 for the values obtained in this study for Tana
1162 quartzite. Results from published studies are included for comparison.

1163 Figure 16. Sketch of the grain assemblage evolution during deformation.

1164 Table 1. Grain parameters for starting material Tana quartzite calculated from
1165 segmentation of both cross-polarized (CP) and cathodoluminescence (CL) light
1166 microscopy images. D_{eq} is the equivalent diameter (diameter of a circle of the same

1167 area than the grain) and AR is the Aspect Ratio (ratio of major and minor axes of the
1168 ellipse fitting).

1169 Table 2. Experimental conditions of deformed samples.

1170 Table 3. Flow stresses obtained and corresponding strain rates for the two strain rate
1171 stepping experiments performed.

1172 Table 4. Results from particle analysis. The errors correspond to the standard
1173 deviation.

1174 Table 5. Results from SURFOR analysis. For the finite sample strain, the first column
1175 corresponds to the calculated strain and the second column to the measured strain
1176 (refer to Table 2. for details).

1177 Table 6. Grain sizes obtained from EBSD analysis on 546LN (1000 MPa) and OR56
1178 (2000 MPa, high-strained) samples (corresponding maps in Figs.11 & 12).

Table 1. Grain parameters for starting material Tana quartzite calculated from segmentation of both cross-polarized (CP) and cathodoluminescence (CL) light microscopy images. D_{eq} is the equivalent diameter (diameter of a circle of the same area than the grain) and AR is the Aspect Ratio (ratio of major and minor axes of the ellipse fitting).

	d_{eq} (µm)	**AR**	**d_{eq} (µm)**	**AR**
	CP-image analysis		LM-CL-image analysis	
N	1423		2103	
Mean	203.71	1.56	186.18	1.55
Median	198.20	1.47	178.60	1.46
RMS	210.78	-	196.14	-
SD	54.16	0.38	61.72	0.38
Max	451.49	3.54	476.29	4.68
Min	210.78	1.01	57.47	1.01

Table 2. Experimental conditions of deformed samples.

Sample name	Griggs apparatus	Temperature (°C)	Water added (wt.%)	Confining pressure (MPa)	Strain rate (s^{-1})	Shortening calculated (%)	Shortening measured* (%)
542LN	Tromsø	900	0.1	600	1.29E-06	33.46	30.48
544LN				1500	1.37E-06	33.48	30.71
546LN				1000	1.28E-06	31.27	28.01
OR32	Orléans			1000	9.32E-07	30.96	29.39
OR42				800	8.12E-07	29.71	30.83
OR48				1250	8.80E-07	28.42	27.71
OR52				700	8.26E-07	31.98	32.12
OR56				2000	*not determined*		74.43
OR57				2000	*not determined*		27.76
OR60				600	7.33E-07	30.92	30.57
OR62				2000	9.29E-07	30.53	29.51
OR64				1500	9.40E-07	29.76	26.59
OR59				1000	Hot pressed (251.7h)		0.53
OR66				2000	Hot pressed (216.8h)		-
OR68				2000	Strain rate stepping		
OR79				800	Strain rate stepping		

*error is estimated to be up to 0.8% for a measuring error of 0.1 mm

Table 3. Flow stresses obtained and corresponding strain rates for the two strain rate stepping experiments performed.

Sample	**OR68**	**OR79**
Pressure (MPa)	2000	800
Temperature (°C)	900	
Diff. stress at 10^{-5} s^{-1}	200.6	471.7
Diff. stress at 10^{-6} s^{-1}	85.4	164.3
Diff. stress at 10^{-7} s^{-1}	*10.0*	*65.3*
Diff. stress at 10^{-5} s^{-1}	265.2	633.4

Table 4. Results from particle analysis. The errors correspond to the standard deviation.

Sample	Confining pressure (MPa)	Number of grains analysed	Equivalent diameter (μm)	Aspect Ratio
TQ2	Starting material	2103	186 ± 62	1.55 ± 0.38
OR52	700	2203	174 ± 62	1.95 ± 0.64
546LN	1000	1116	230 ± 69	1.76 ± 0.54
OR32	1000	1835	204 ± 69	2.05 ± 0.73
OR64	1500	2603	172 ± 54	1.81 ± 0.55
OR62	2000	3072	181 ± 66	1.85 ± 0.57

Table 5. Results from SURFOR analysis. For the finite sample strain, the first column corresponds to the calculated strain and the second column to the measured strain (refer to Table 2. for details).

Sample	Confining pressure (MPa)	Minimum of the projection curve	Angle of minimum (°)	Angle(s) of maximum (°)	Fabric anisotropy (%)	Finite sample strains (%) Calc.	Meas.
TQ2	Starting material	0.965	70	160 – 165	3.5	-	
OR52	700	0.656	90	0 – 175	34.4	31.98	32.12
546LN	1000	0.754	85	170 – 175	24.60	31.27	28.01
OR32	1000	0.628	90	0 – 180	37.2	30.96	29.39
OR64	1500	0.722	80	170	27.8	29.76	26.59
OR62	2000	0.718	85	170 – 175	28.2	30.53	29.51

Table 6. Grain sizes obtained from EBSD analysis on 546LN (1000 MPa) and OR56 (2000 MPa, high-strained) samples (corresponding maps in Figs.11 & 12).

	546LN			OR56		
	Relict grains	**Recryst. grains**	**Subgrains**	**Relict grains**	**Recryst. grains**	**Subgrains**
Arith. Mean	7.967	3.789	3.854	9.030	3.323	2.683
Geom. Mean	7.595	3.291	2.884	8.314	2.825	2.121
RMS	8.613	4.282	4.879	9.853	3.824	3.871
Median	7.930	3.450	3.230	8.091	2.968	2.252
Mode	7 – 8	3.5 – 4 4.5 – 5	4 – 4.5	7 – 9	3.2 – 3.6	1.5 – 1.7
Std. Dev.	2.603	2.003	2.993	3.955	1.894	2.790

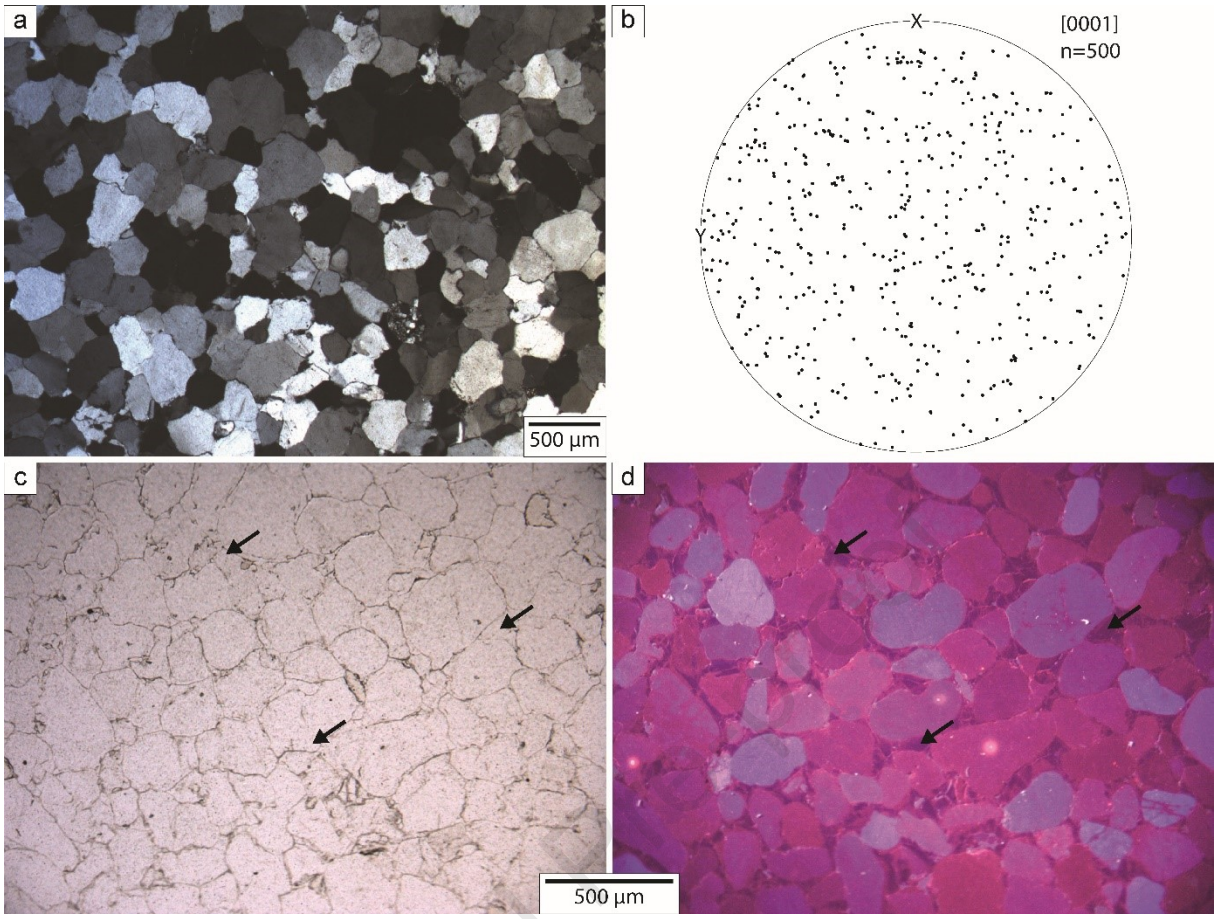

Figure 1. (a) Cross-polarized microphotograph of starting material Tana quartzite showing equant grains without undulatory extinction. (b) Pole figure of random crystallographic orientation of c-axis from 500 grains measured by EBSD. (c & d) Plane polarized light microscope-cathodoluminescence images: equant and rounded sand grains of various tints are surrounded by darker cement that grows in crystallographic continuity (arrows).

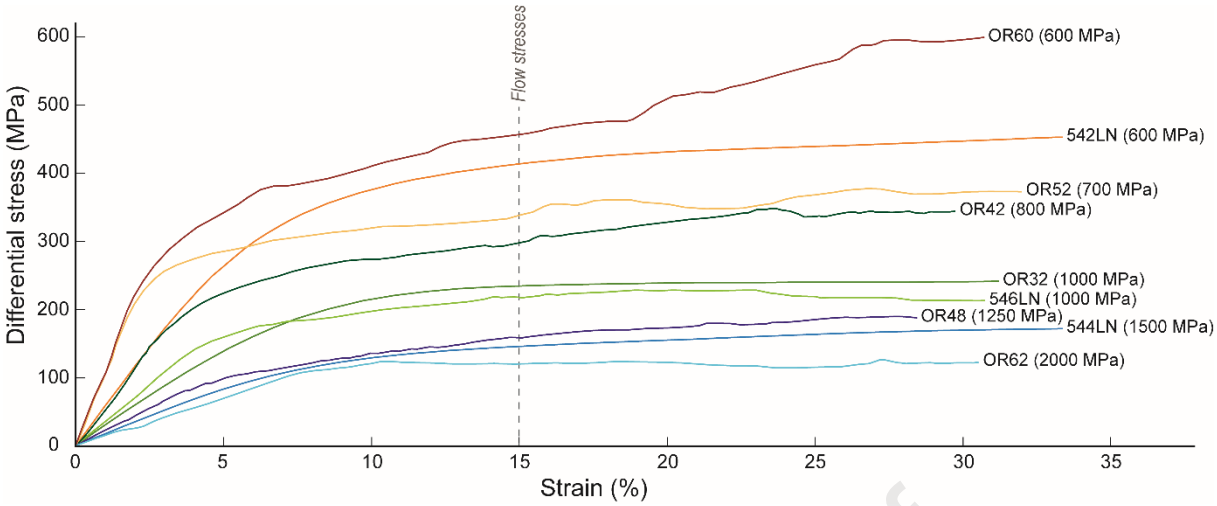

Figure 2. Mechanical data for samples deformed in wet conditions (0.1 wt.% H2O added) at 900°C for confining pressures between 600 and 2000 MPa. Samples …LN have been deformed in Tromsø (Norway) whereas samples OR… have been deformed in Orléans (France). The samples strengths systematically decrease with increasing confining pressure.

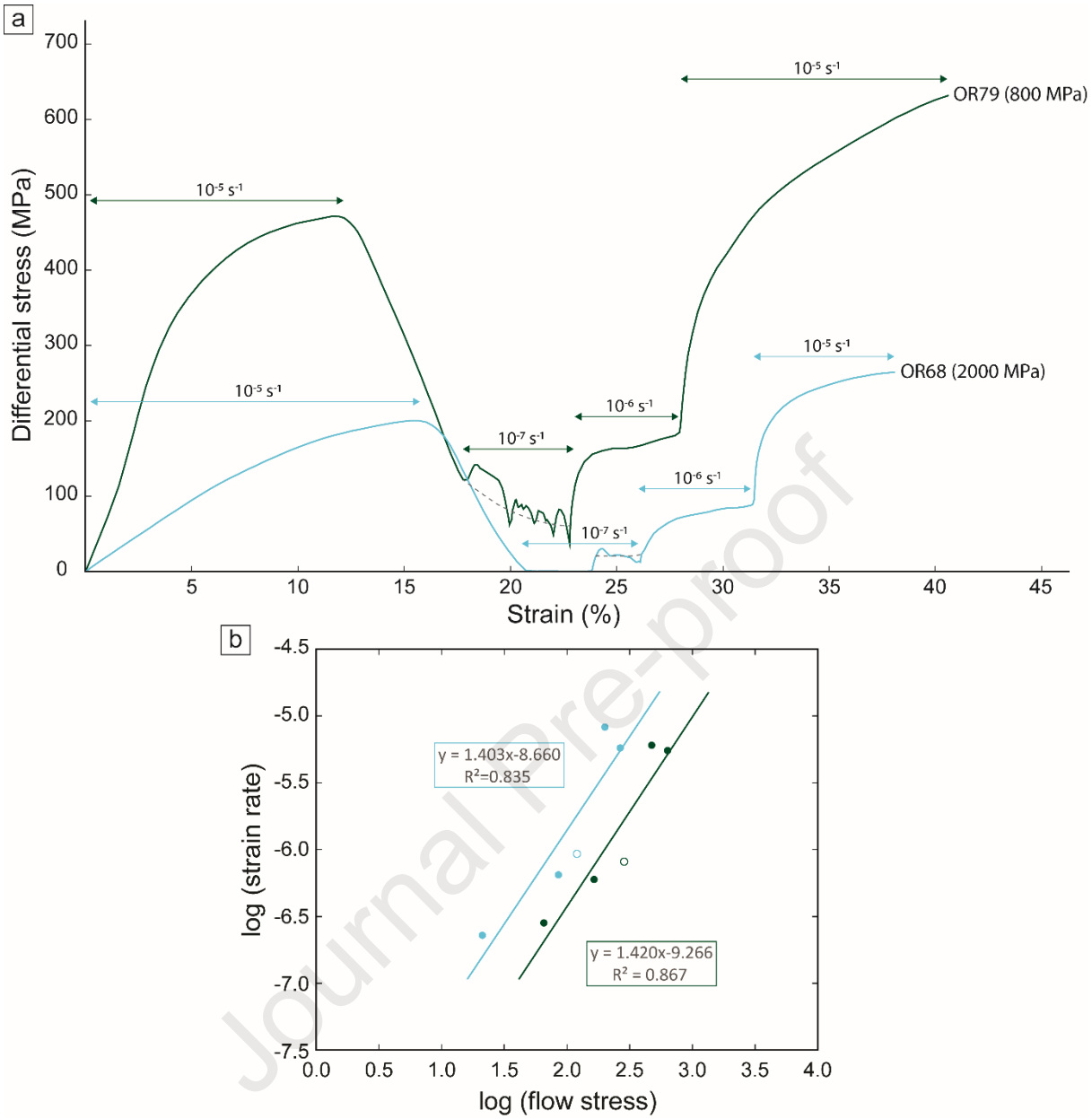

Figure 3. (a) Stress strain curves obtained for strain rate stepping experiments at 800 MPa (OR79) and 2000 MPa (OR68). (b) Plot of the log strain rate vs. log flow stress. Solid circles are data obtained from strain rate stepping experiments whereas open circles are data from samples deformed at 10^{-6} s^{-1} constant strain rate at the same confining pressures. The slopes of the regressed lines indicate n-values of ~1.89 at 2000 MPa and ~2.06 at 800 MPa.

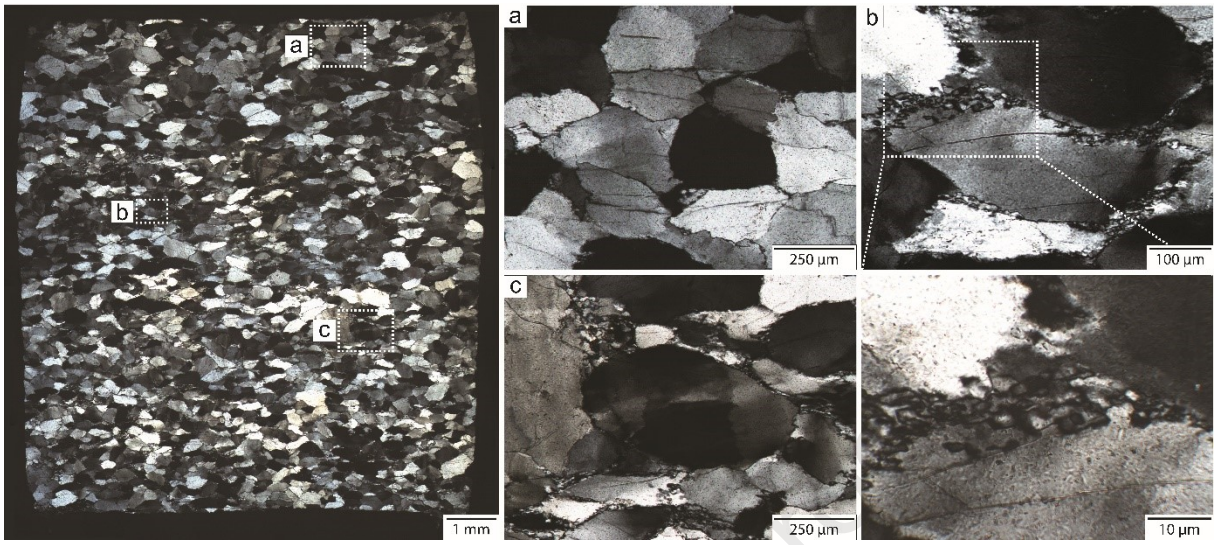

Figure 4. Cross polarized light images of sample OR32 deformed at 1000 MPa confining pressure. Left: overview of sample showing higher strain regions near the centre of the sample. In the most strongly deformed part of the sample, clasts are elongated, and limited recrystallization is observed at grain boundaries (core-mantle structures). Right: details of the recrystallized region showing undulatory extinction, subgrains, and new grains. The shortening direction is vertical.

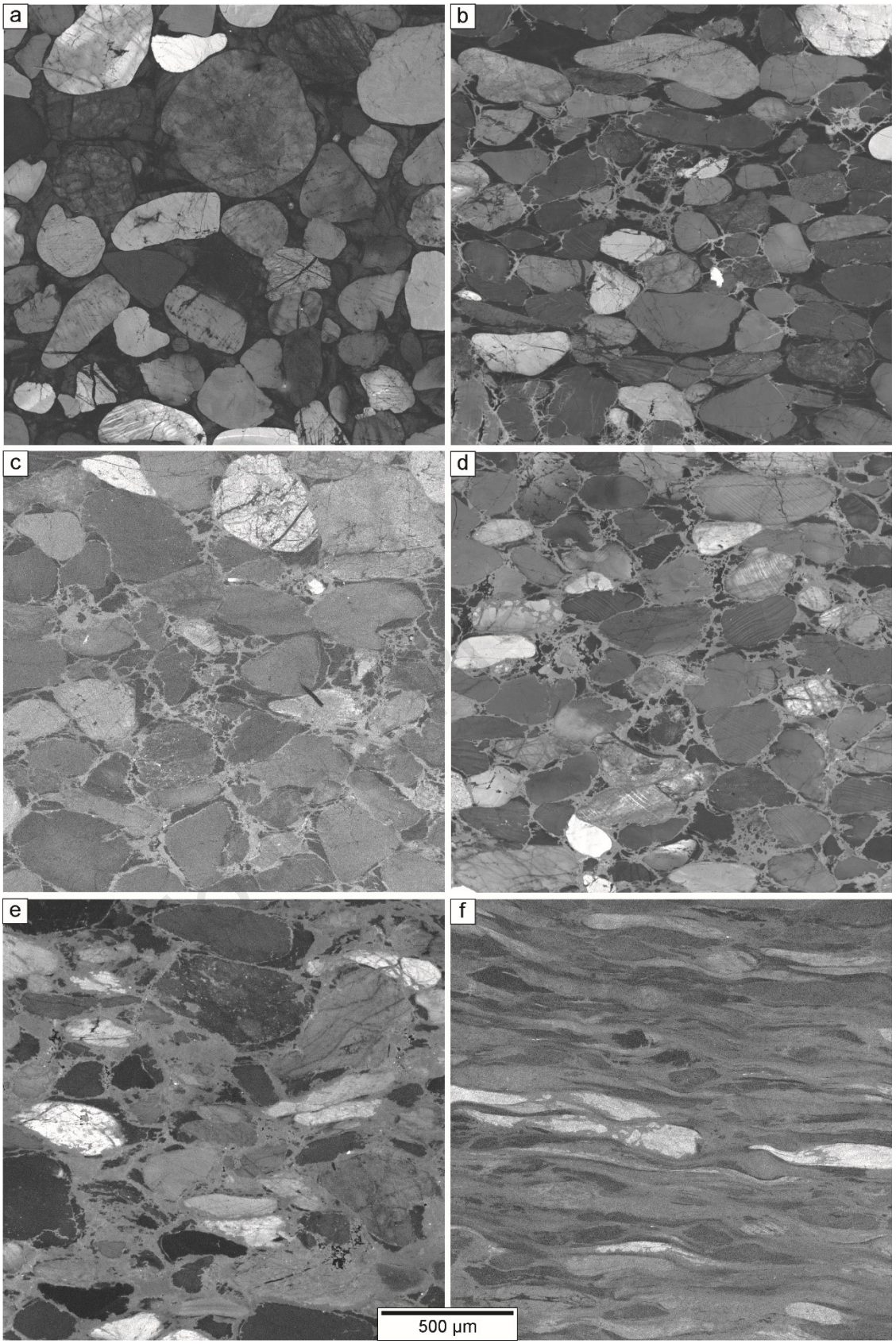

Figure 5. SEM-cathodoluminescence images of (a) starting material and of samples deformed at confining pressure of (b) 700 MPa (OR52), (c) 1000 MPa (546LN), (d) 1500 MPa (OR64), (e) 2000 MPa (OR62) and (f) 2000 MPa high-strain (74%; OR56). The shortening direction is vertical for images (b-f).

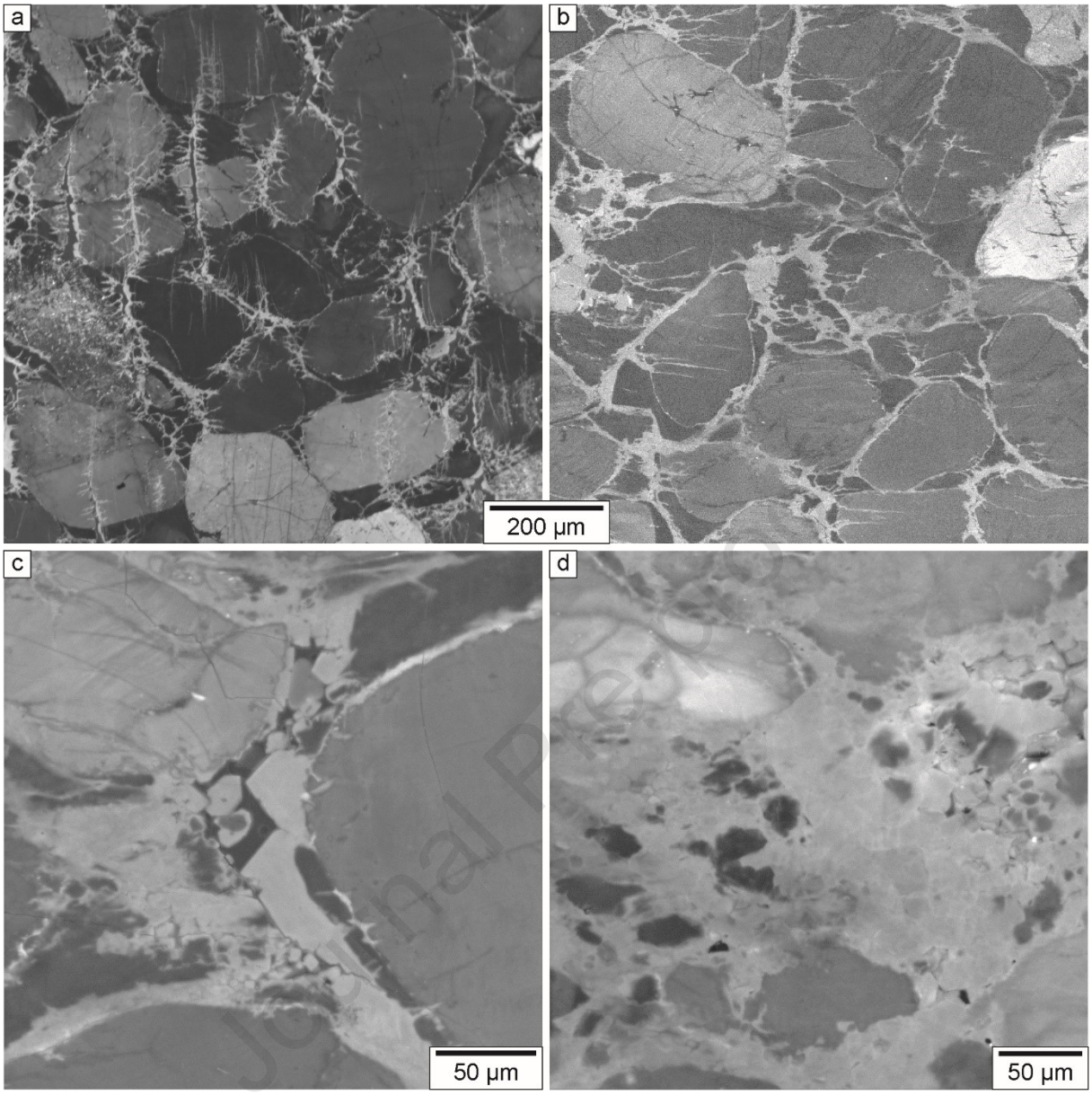

Figure 6. (a & b) SEM-CL-images of cracks in both cement and grains in sample deformed at (a) 800 (OR42) and (b) 1000 MPa (546LN) confining pressure. (c) Crystal faces at open grain boundary region in 546LN sample (1000 MPa). (d) Crystal faces in small luminescent grains in open space between grains in OR64 sample (1500 MPa). The shortening direction is vertical for all images.

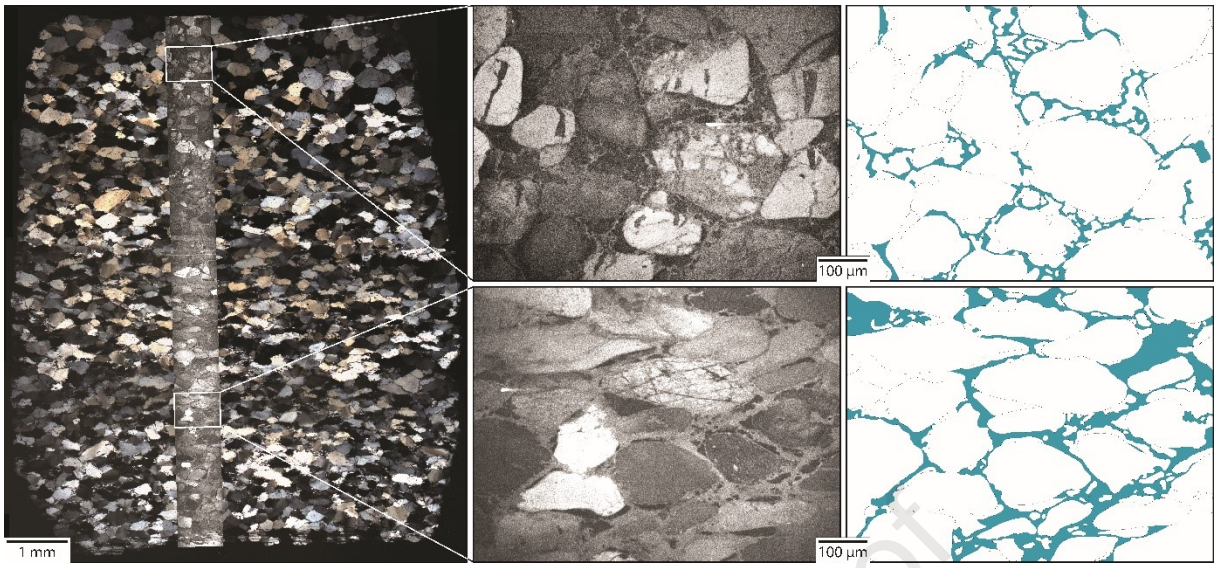

Figure 7. Left: mosaic of OR57 sample (2000 MPa) in polarized light with associated SEM-CL-images longitudinal transect. Right: examples of segmentation and identification of bright luminescent zones (coloured in blue).

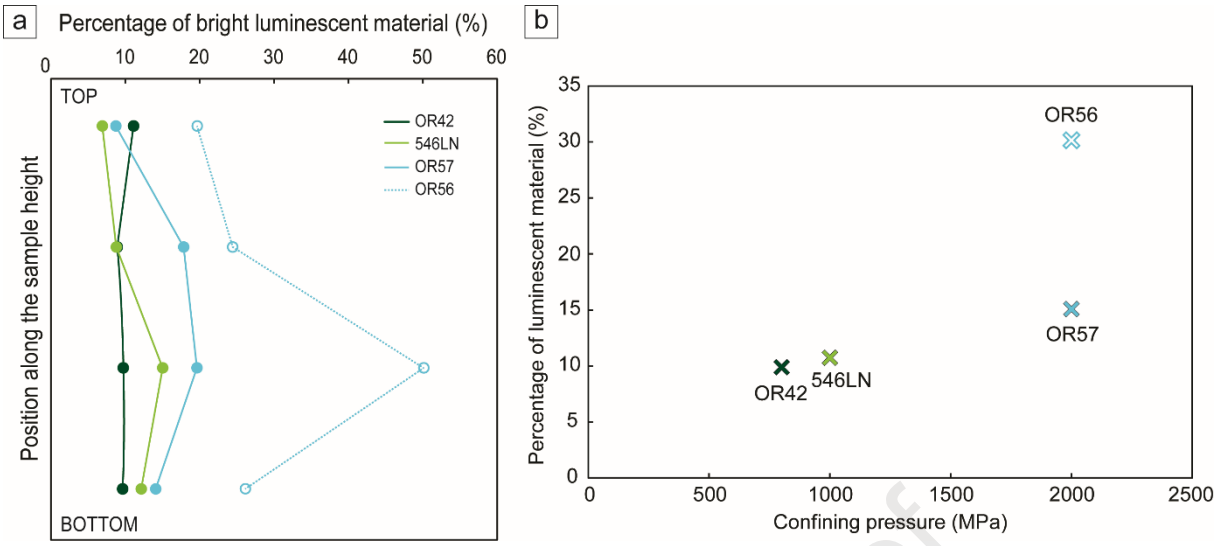

Figure 8. Percentage of bright luminescence for SEM-CL images longitudinal transects, (a) as a function of the position along the sample and (b) as a function of the confining pressure.

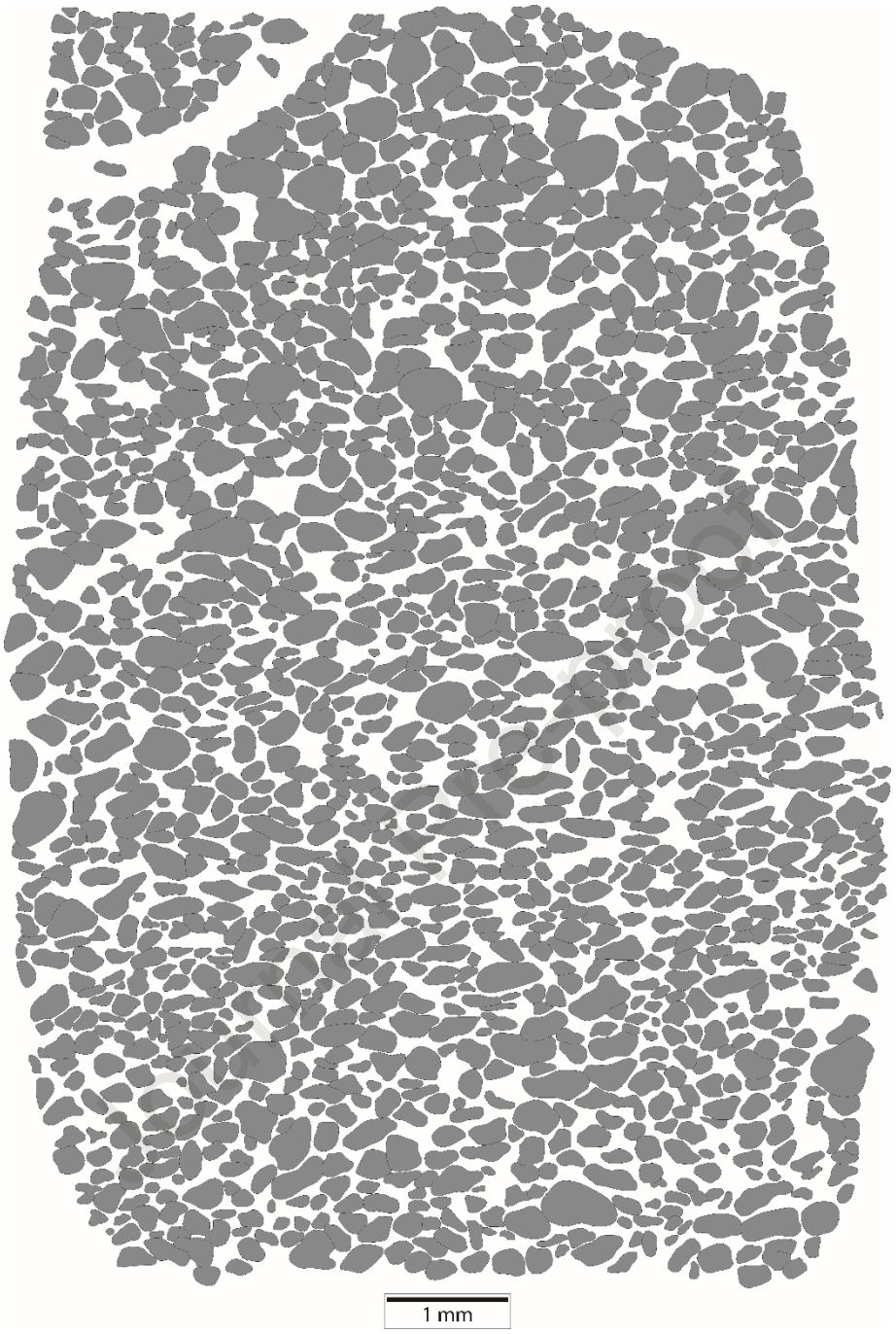

Figure 9. Example of the manual segmentation made for the OR62 (2000 MPa) thin section from optical cathodoluminescence images. Interiors of grains are isolated from the surrounding cement based on their luminescence colour contrasts. The shortening direction is vertical.

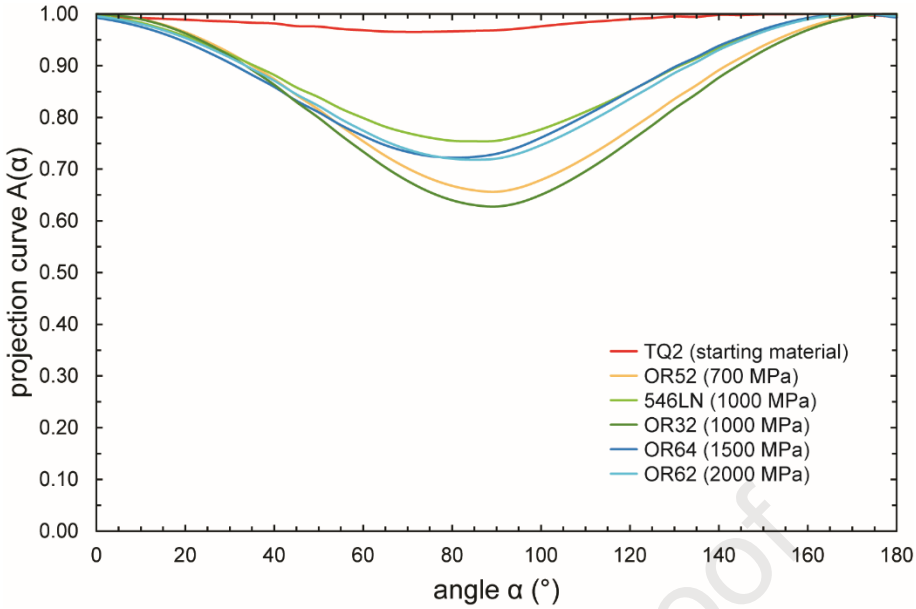

Figure 10. SURFOR projections curves showing that the starting material TQ2 has a slight strain of 3.5% whereas deformed samples at various confining pressures have an orientation comprise between 80 and 90° for a strain comprise between 24.6% (546LN) and 34.4% (OR52). The global shortening direction for deformed samples is theoretically 90°.

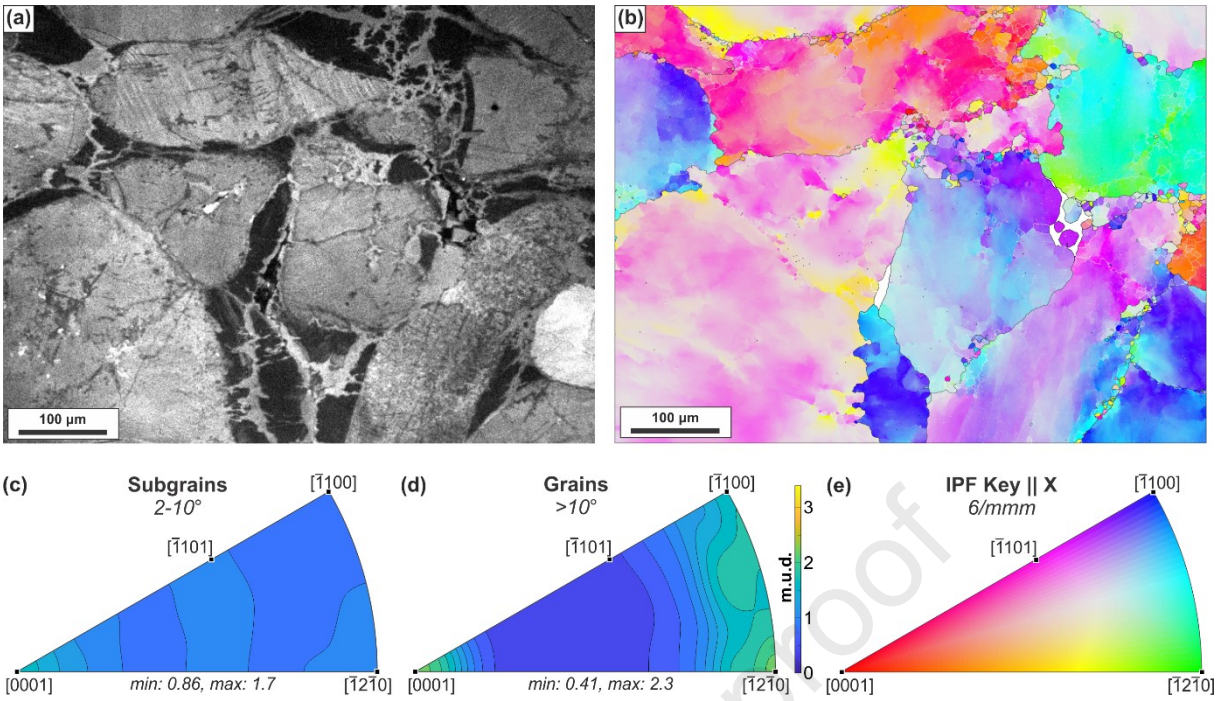

Figure 11. Cathodoluminescence (CL) image, EBSD orientation map and inverse pole figures (IPF) for sample 546LN. (a) CL image with blue (380-515 nm) optical filter to highlight recrystallized areas; (b) EBSD map of quartz orientations coloured parallel to the X direction, sample is plotted with hexagonal symmetry (6/mmm) to account for the effect of Dauphiné twins. Grain boundaries are identified by black bounding lines and subgrains are identified by white boundaries. (c) IPF's for subgrain (defined by a misorientation between 2 and 10°) boundaries and (d) grain (defined by a misorientation greater than 10°) boundaries. All IPF's are plotted in hexagonal 6/mmm symmetry with the same scale for multiples of uniform (m.u.d.) for each plot. (e) Colour key for IPF ǁ X map.

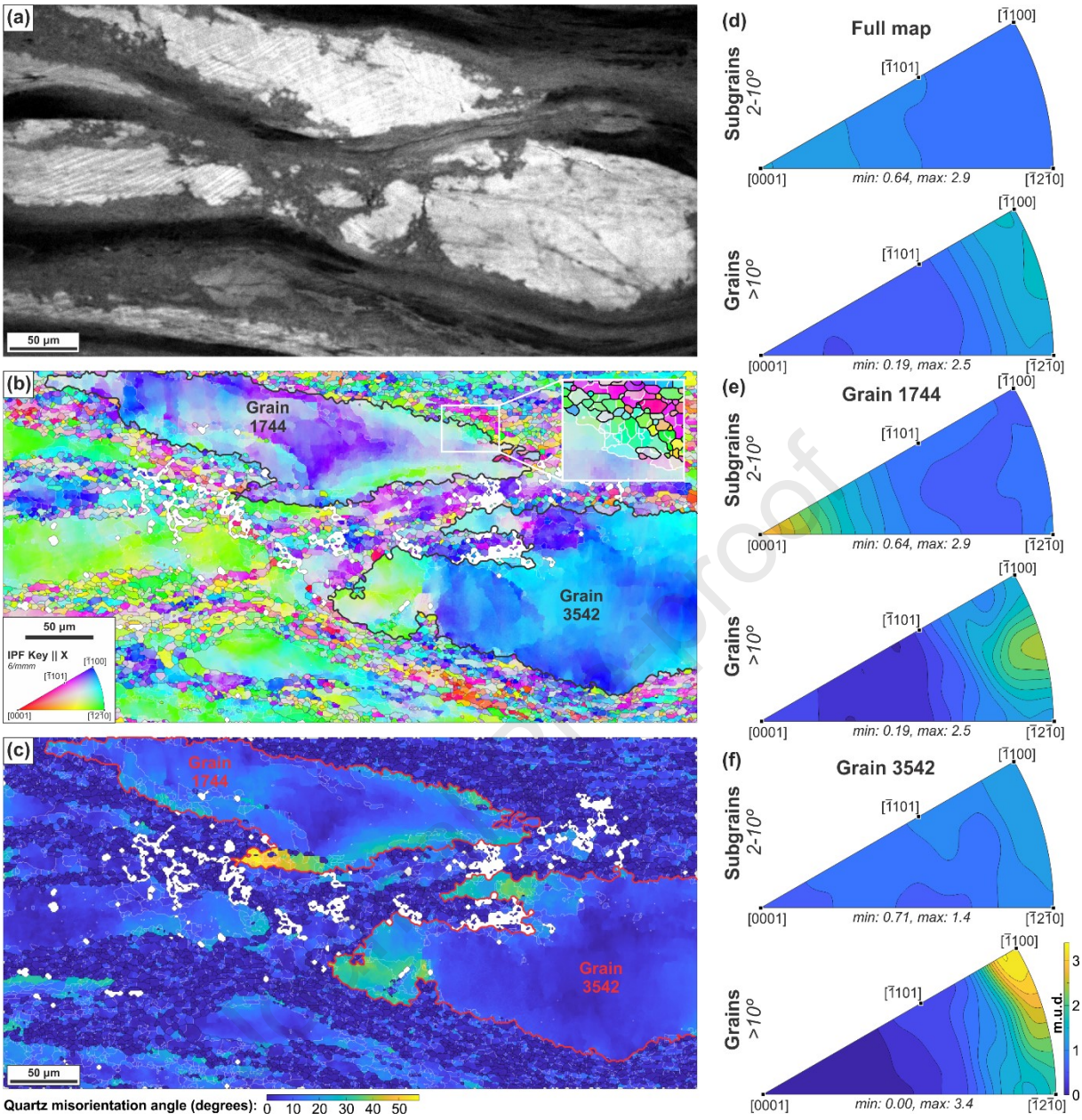

Figure 12. Cathodoluminescence (CL) image, EBSD orientation map, misorientation map and inverse pole figures (IPF) for high strain sample OR56. (a) CL image with blue (380-515 nm) filter to highlight recrystallized areas. (b) EBSD map of quartz orientations coloured parallel to the X direction, sample is plotted with hexagonal symmetry (6/mmm) to account for the effects of Dauphiné twins. Grain boundaries are identified by black bounding lines and subgrains are identified by white boundaries (see detailed insert at the top right hand corner). (c) Misorientation map where blue shows low misorientation and yellow shows high misorientation relative to the mean grain orientation. Grains 1744 and 3542 are highlighted on the IPF (bold black) and misorientation (red) maps. (d-f) IPF's for subgrain (defined by a misorientation between 2 and 10°) and grain (defined by a misorientation greater than 10°) boundaries with the d) full map, (e) grain 1744 and (f) grain 3542. All IPF's are plotted in hexagonal 6/mmm symmetry with the same scale for multiples of uniform distribution (m.u.d.) for each plot.

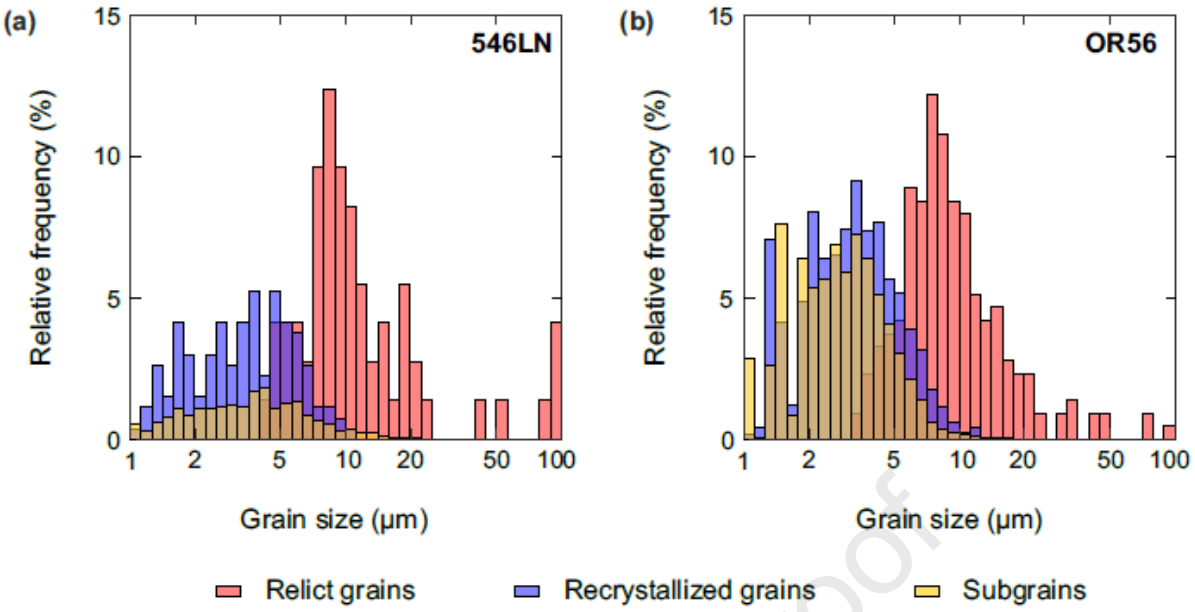

Figure 13. Log_{10} grain size distributions for samples (a) 546LN and (b) OR56. Grain size distributions are separated into relict, recrystallized and subgrain populations.

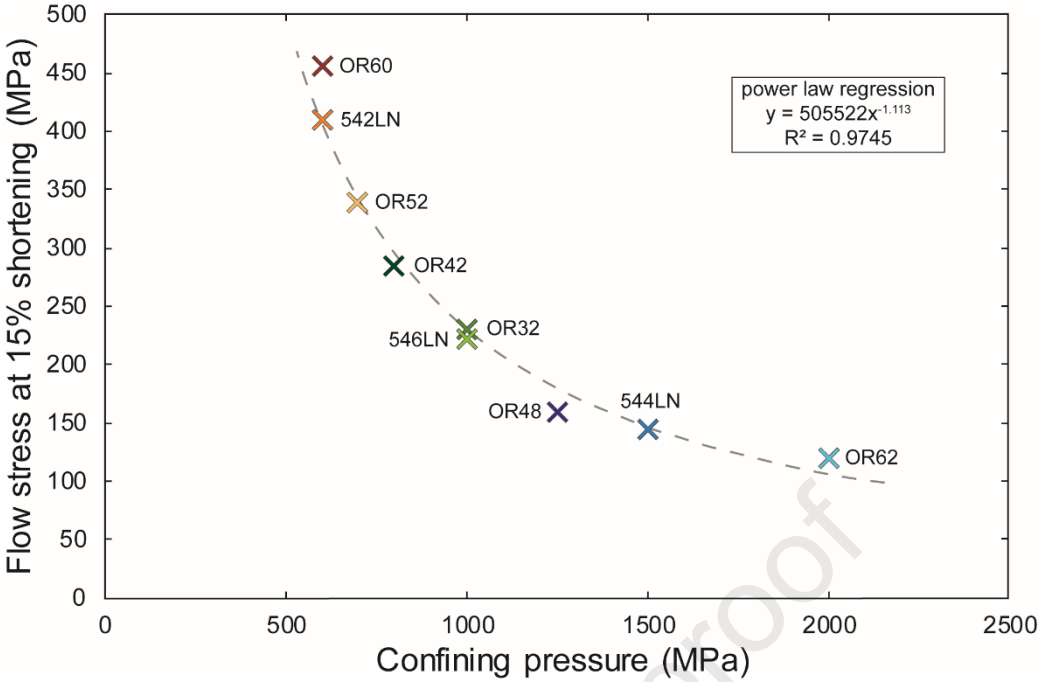

Figure 14. A power-law relationship fitted to the flow stresses (at 15% strain) at different confining pressures.

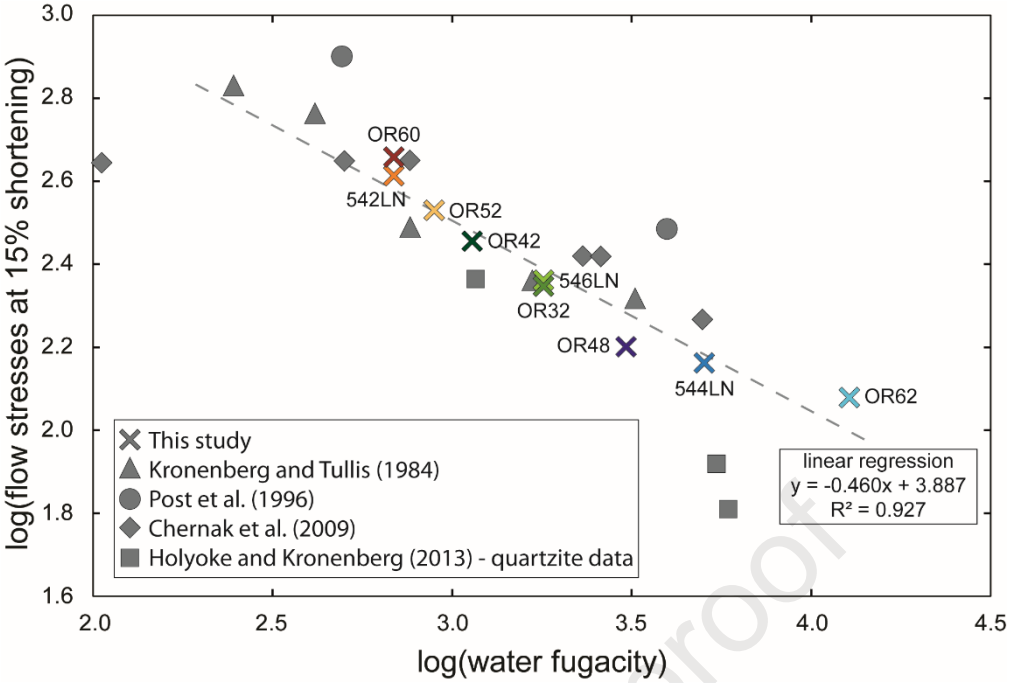

Figure 15. Relationship between water fugacity and flow stresses. The slope indicates a m/n coefficient of 0.46 for the values obtained in this study for Tana quartzite. Results from published studies are included for comparison.

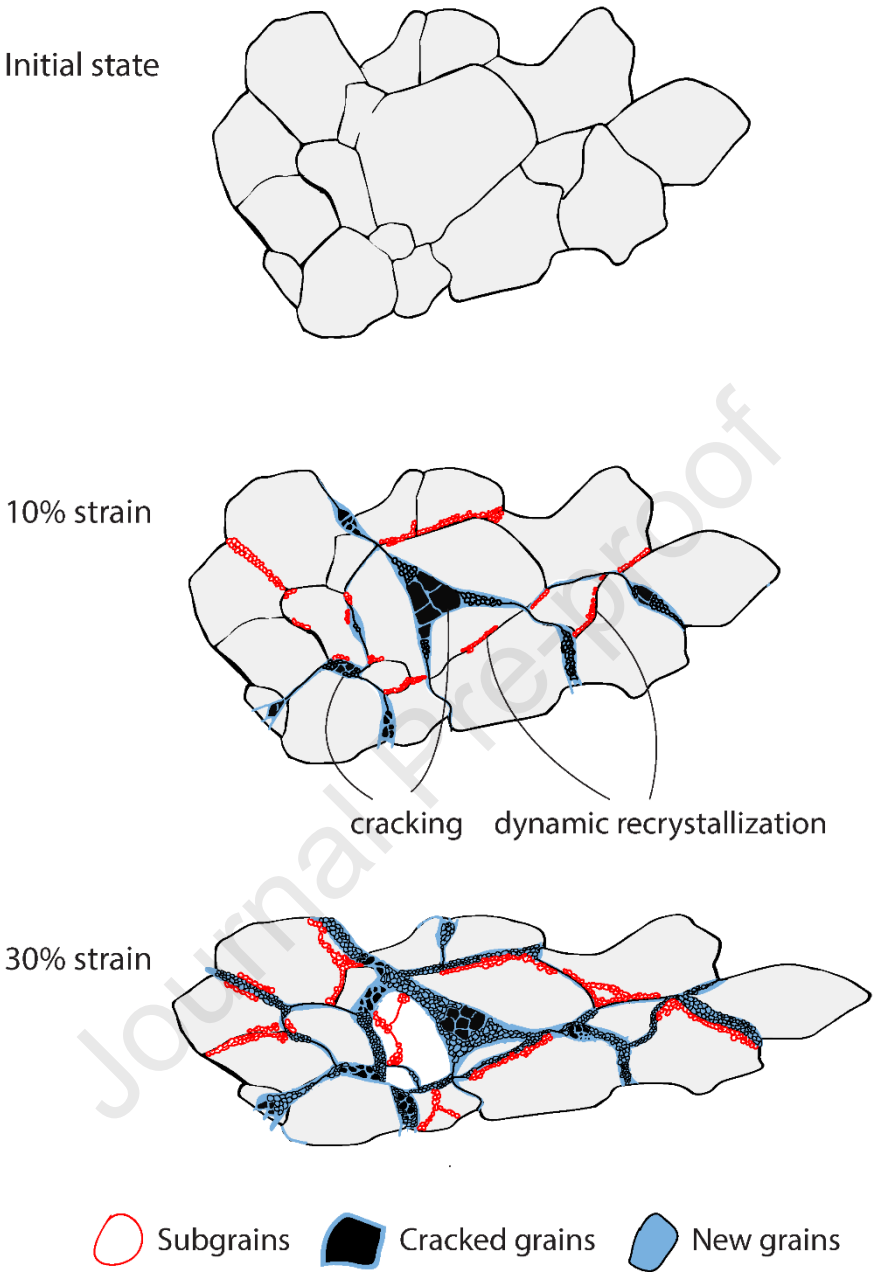

Figure 16. Sketch of the grain assemblage evolution during deformation.

Highlights

Inverse pressure dependence of flow stress in experimentally deformed quartzite

Bulk strain is accommodated by grain crystal plasticity

Recrystallization results from combined subgrain rotation and mode I cracking

Recrystallization processes are discriminated using cathodoluminescence of quartz

Pressure enhances grain boundary migration and reduces flow stress

Declaration of interests

☒ The authors declare that they have no known competing financial interests or personal relationships that could have appeared to influence the work reported in this paper.

☐The authors declare the following financial interests/personal relationships which may be considered as potential competing interests: